



Petrographic and chemical characterization and carbon and nitrogen isotopic compositions of cometary IDPs and their GEMS amorphous silicates

Birgit Schulz^{a,*}, Christian Vollmer^a, Jan Leitner^{b,c}, Lindsay P. Keller^d, Quentin M. Ramasse^{e,f}

^a Institut für Mineralogie, Universität Münster, Corrensstr. 24, 48149 Münster, Germany

^b Institut für Geowissenschaften, Ruprecht-Karls-Universität Heidelberg, Im Neuenheimer Feld 234-236, 69120 Heidelberg, Germany

^c Max-Planck-Institut für Chemie, Hahn-Meitner-Weg 1, 55128 Mainz, Germany

^d XI3, Astromaterials Research and Exploration Science (ARES) Division, NASA Johnson Space Center, Houston, TX 77058, United States

^e SuperSTEM Laboratory, SciTech Daresbury Campus, Daresbury WA4 4AD, UK

^f School of Chemical and Process Engineering, School of Physics and Astronomy, University of Leeds, Leeds LS2 9JT, UK

ARTICLE INFO

Associate editor: Hikaru Yabuta

Keywords:

Interplanetary dust particles
GEMS
Amorphous silicates
Transmission electron microscopy

ABSTRACT

GEMS (glass with embedded metal and sulfides) are the dominant carrier of amorphous silicates in anhydrous interplanetary dust particles (IDPs) and one of the most suitable materials to study early solar system processes. Amorphous silicates in 105 GEMS from eight IDPs were analyzed regarding texture and chemical composition to reassess GEMS formation theories and genetic relationships to amorphous silicate material in meteorites. Petrography of bulk IDPs was investigated to understand GEMS' relationships to other IDP components. Furthermore, carbon and nitrogen isotopic compositions were measured. Nearly all GEMS are aggregates of several subgrains with variable amount of nanophase inclusions and different Mg- and Si-contents, while single GEMS are rare. The subgrains within aggregates are typically surrounded by one or more carbon rims with high density. The chemical compositions of GEMS amorphous silicates are subsolar for all major element/Si ratios but exhibit wide heterogeneity. This is not influenced by silicon oil from the capturing process of IDPs as assumed before, as a penetration of the silicon oil is excluded by high resolution EELS (electron energy loss spectroscopy) areal density maps of silicon. Furthermore, low Fe-content in GEMS amorphous silicates shows that these are not altered by aqueous activity on the parent body as it is the case for amorphous silicate material in primitive meteorites. The subsolar element/Si ratios and the wide chemical heterogeneity point to a non-equilibrium fractional condensation origin either in the early solar nebula or in a circumstellar environment and are not in agreement with homogenization via sputtering in the ISM. The close association with carbon around GEMS subgrains and as double-rims around GEMS aggregates argue for a multi-step aggregation after formation of the smallest GEMS subgrains in the ISM or the early solar nebula. Carbon acting as matrix material connecting GEMS and other IDP components has lower areal density as seen from carbon EELS areal density maps and isotopic anomalies varying at the nanometer scale, pointing to different origins and processing of materials to varying extent or at changing temperatures.

To balance GEMS' subsolar element/Si ratios, a supersolar component in IDPs was assumed to account for the overall chondritic composition of bulk IDPs. Nevertheless, our bulk IDP analyses revealed subsolar, but variable, element/Si ratios for complete particles as well, depending on type and amount of mineral phases in each particle. Pyroxenes in the investigated particles can occur as elongated euhedral crystals, but are overall rare. The dominant crystalline fraction in the investigated IDP samples are equilibrated aggregates (EAs) that show the same chemical compositions as GEMS, indicating that the EAs are recrystallized GEMS grains and formed after GEMS formation as secondary phases.

* Corresponding author.

E-mail address: b_schu64@uni-muenster.de (B. Schulz).

<https://doi.org/10.1016/j.gca.2024.06.013>

Received 14 March 2023; Accepted 17 June 2024

Available online 19 June 2024

0016-7037/© 2024 The Author(s). Published by Elsevier Ltd. This is an open access article under the CC BY license (<http://creativecommons.org/licenses/by/4.0/>).

1. Introduction

Amorphous silicates in extraterrestrial samples are very important objects to investigate early solar system history and processes in the solar nebula. Due to their metastable structure, they are highly susceptible to alteration, which means that their preservation is an excellent indicator that the sample escaped strong thermal or aqueous alteration. Therefore, they are often considered to be the primary building blocks of all solid objects in our solar system. Amorphous silicates are described from the matrices of very primitive meteorites like the ungrouped carbonaceous chondrite Acfer 094 (Greshake, 1997; Hopp and Vollmer, 2018), CR, CO, and CM chondrites (Abreu, 2016; Abreu and Brearley, 2010; Le Guillou et al., 2015; Leroux et al., 2015; McAdam et al., 2018; Ohtaki et al., 2021; Vollmer et al., 2020), or unequilibrated ordinary chondrites (Dobrić and Brearley, 2020), and from the matrix of GEMS (glass with embedded metal and sulfides) in anhydrous interplanetary dust particles (IDPs) (Bradley, 1988).

IDPs are 5–50 μm sized objects (Bradley, 1988; Flynn, 1996). Because of their small size, they survive atmospheric entry without severe damage and can be collected from Earth's stratosphere by NASA aircrafts with special collectors in high quantity (Brownlee, 1985). Specifically, anhydrous IDPs are considered to have never experienced any aqueous alteration because they are thought to originate mostly from Kuiper Belt or Oort cloud comets beyond the snowline (Brownlee, 2014; Keller and Flynn, 2022). The majority of IDPs have an overall chondritic composition and are subdivided into the chondritic-porous (CP) and the chondritic-smooth (CS) subset. CS-particles contain hydrated layer-lattice silicates like serpentine and smectite while CP-IDPs are dominated by the anhydrous silicate minerals Mg-rich pyroxene or olivine with only minor signs of aqueous alteration, such as the presence of nickel-, zinc-, or copper-iron sulfides, as described from comet 81P/Wild 2 (Berger et al., 2011; Bradley, 2014). Pyroxenes sometimes exhibit elongated morphologies described as whisker-like, which are thought to be indicative of vapor-phase growth (Bradley et al., 1983). IDPs also contain Fe-Ni-sulfides (pyrrhotite, pentlandite), Fe-Ni-metal (kamacite, taenite), magnetite, so-called equilibrated aggregates (EAs, irregularly shaped, polycrystalline silicate grains (Keller and Messenger, 2009)), and GEMS grains, all embedded in a semi-continuous matrix of carbonaceous material (Bradley, 1988; Bradley, 2014). EAs are often thought to have formed from recrystallized GEMS (Keller and Messenger, 2009).

Bradley (1994) defined GEMS as polyphase grains of sizes between 100 and 500 nm in diameter with a silicate glass matrix and inclusions of Fe-Ni-metal (kamacite) and Fe-sulfides (pyrrhotite). They are rounded to irregular objects, and occur isolated, in clusters of two or more individual grains stuck together by carbonaceous material, or as diffuse areas (Ishii, 2019). Bulk GEMS have chondritic composition within a factor of 3 for most major elements, but are heterogeneous at the nanometer scale (Bradley, 1988). They are typically surrounded by organic carbon or contain carbon around smaller subgrains in aggregate GEMS (Ishii et al., 2018). GEMS are either thought to have formed by irradiation of crystalline precursor grains in the interstellar medium (ISM) (Bradley and Dai, 2004) or condensed directly from the solar nebula or in the outflows of AGB stars via non-equilibrium condensation (Keller and Messenger, 2011). GEMS are therefore one of the most primitive components of the early solar nebula.

It is still not well constrained, to what extent amorphous silicates in GEMS differ from amorphous silicate material (ASM) in carbonaceous chondrite matrices and whether compositional and textural similarities or differences reflect different formation histories or secondary processes. Recent studies indicate that GEMS-like material in meteorites such as Paris or Acfer 094 is unlike GEMS in IDPs because of a higher degree of partial ordering, more Fe-enriched chemical compositions and higher Fe oxidation states in the GEMS-like material (Ohtaki et al., 2021; Villalon et al., 2021). Furthermore, nanophase metal inclusions are rare in meteorite ASM, while they are a major constituent of GEMS in IDPs. Nevertheless, it is not clear, whether these characteristics are a result of

alteration of GEMS or whether the GEMS-like material has a completely different formation history. Furthermore, the investigation of the GEMS' host IDPs petrography is important to constrain possible genetic relationships to other IDP components and to elucidate the processes that might have affected IDPs. This is crucial to constrain the physico-chemical conditions of IDP formation and to reconstruct processes in the solar nebula or the interstellar medium.

Up to now, only individual IDPs have been investigated (Keller, 2020) and it is of particular interest to determine the percentage and distribution of phases among different IDPs. Therefore, in this work, eight different IDPs have been investigated regarding texture, mineralogy, carbon and nitrogen isotopic compositions, bulk chemical composition and chemical composition of different mineral phases using transmission electron microscopy (TEM) and Nanoscale-secondary ion mass spectrometry (Nano-SIMS), to shed new light on the longstanding controversy about GEMS formation hypotheses and their role in early solar system processes.

2. Samples and methods

2.1. Preparation of IDP samples

Eight IDPs from several collectors were chosen for analysis. Details to selected IDPs are given in [Tab. S1 in the supplementary material](#). Particles were selected based on their preliminary EDX spectra classifying them as overall chondritic, and on their Fe/S ratio. Fe/S ratios lower than CI indicate loss of volatiles due to atmospheric entry heating of IDPs. Allocated particles are all fine-grained, anhydrous, and are assigned to the chondritic-porous subset of IDPs.

The particles were embedded in epoxy after cleaning them with hexane to remove silicon oil from the capturing process, and then cut into 50–70 nm thin sections using ultramicrotome facilities at NASA-JSC and the University of Münster. Thin sections were then placed on Cu-TEM-grids with amorphous carbon support films. For each particle, several grids were prepared, but not all of them contained particle sections. Initial documentation of grids was performed using a JEOL JSM 6510-LA Scanning Electron Microscope in secondary electron imaging mode (20 kV, Tungsten filament), which allowed numbering and location of sections on TEM grids. Additionally, particles on grid bars unsuitable for TEM analysis could be identified for later NanoSIMS analysis.

2.2. Transmission Electron Microscopy

Particles were initially characterized with a Zeiss Libra 200FE TEM (200 kV) equipped with a Schottky field emission gun and an in-column Omega energy filter using conventional bright-field (BF) imaging. BF imaging gives information about crystallinity of phases by using only transmitted electrons for imaging, which allows distinction between crystalline and amorphous parts in the particles. BF images were also utilized to measure sizes of complete particles and the pore space in individual sections using Gatan's GMS3.5 software suite (Gatan Ametek Inc., Pleasanton, USA). Main investigations were performed with a Titan Themis G3 300 TEM (ThermoFisher/FEI) equipped with a Schottky field emission gun (X-FEG), a Wien-type monochromator, a spherical aberration (C_s) corrector in the objective system, a fast CMOS camera (Ceta 4k \times 4k), a Fischione Model 6000 high-angle annular dark field (HAADF) detector for scanning TEM (STEM) Z-contrast imaging, and a four-quadrant energy-dispersive X-ray (EDX) detector (Super-X G2) for EDX analysis. For EDX mapping, a full EDX spectrum was collected on each pixel of the selected imaging area and stored in spectrum imaging files (SI) for later analysis, which allows the user to extract chemical information for handpicked areas from the map. Chemical analysis of bulk interplanetary dust particles is challenging since EDX mapping had to be performed over long timescales to get count rates sufficient for quantification. The longer the mapping procedure, the more damage of

the fragile sample is observed. Furthermore, IDPs belonging to the chondritic-porous subset exhibit a high fraction of pore space which was mostly excluded by quantifying handpicked areas in the Thermo Fisher Scientific Velox™ software. For bulk particle chemical compositions, several sections of each particle were mapped, from which average composition was calculated. Statistical errors are 1σ standard deviation from the dataset, except for IDP L2099 A7, for which only one section was usable for mapping. In this case the error from the Thermo Fisher Scientific Velox™ software based on simple counting statistics was used. For the atomic fraction quantification in Velox, the deconvolution error is combined with an error estimate for the cross-section models. Manually picking ROIs also allows it to select truly amorphous silicates inside GEMS and quantify their chemical compositions and to exclude most nanophase inclusions of metals and sulfides. The ThermoFisher Velox™ software uses standard Cliff-Lorimer (k-factor) quantification with absorption correction for EDX quantification. K-factors are taken from the program's database. Absorption is corrected for detector geometry. Compositions are reported in atom percent (at%). Mapping was performed using a ~ 1 nA current to minimize beam damage in the fragile and porous samples. The field of view was chosen to be large enough to cover the complete particle area and typically consisted of 512×512 pixels. Average time for one frame was around 20 s with a dwell time of ~ 50 μ s on each pixel. For each map, between 500 and 800 frames were collected, resulting in total mapping times of 2 to 4 h, depending on size and porosity of the particle in the individual section.

Regions of interest were manually chosen from acquired maps and quantified. Fig. S1 in the supplementary material shows an example of a GEMS aggregate grain with four handpicked ROIs for quantification. ROIs have to be at least around 100 nm in diameter, otherwise, EDX counts are not sufficient for quantification. For EAs or EA areas, ROIs correspond to bulk EA regions, because distinct subgrains inside EAs are not clearly distinguishable. Therefore, those analyses contain mostly recrystallized Mg-rich silicates and minor sulfide crystals. It is not completely possible to avoid nanoinclusions in handpicked areas from EDX maps of GEMS amorphous silicates, because nanoinclusions are as small as 1–2 nm, therefore, approaching single pixel size. Using ultramicrotomed thin sections with thickness of ~ 70 nm avoids nanoinclusions in three-dimensional GEMS grains in depth, and those visible at the surface are then avoided by using handpicked areas from the maps. Ohtaki et al. (2021) also used ultramicrotomed thin sections of IDPs and fine-grained material in meteorites in combination with high spatial resolution EDX mapping, showing the effective exclusion of nanoinclusions during analyses of GEMS amorphous silicates. To further validate our measurements and to make sure that we truly exclude nanophase inclusions in the elemental composition of GEMS amorphous silicates, we used a second step filtering results. The average S/Si value of GEMS amorphous silicates from Ohtaki et al. (2021) is 0.09 ± 0.11 and the average S/Si of bulk GEMS from their analyses is 0.25 ± 0.20 . Therefore, we postfiltered our handpicked EDX regions using the value for GEMS amorphous silicates from Ohtaki et al. (2021) as a cutoff and excluded all analyses with higher S/Si. From 208 datapoints, 105 met this criterium and were validated as representing the chemical composition of the true GEMS amorphous silicates without the nanoinclusions. The combination of using ultramicrotomed thin sections, handpicking regions without nanoinclusions from EDX maps of GEMS, and excluding all analyses with S/Si > 0.09 is therefore the best method to date to obtain chemical composition of GEMS amorphous silicates, although some of the smallest nanoinclusions cannot be avoided completely.

Additional EELS measurements were performed on a Nion Ultra STEM 100MC 'Hermes' at SuperSTEM Laboratory in Daresbury, UK, operated at 60 kV. This instrument is equipped with a C5 Nion QO corrector for high spatial resolution, a 40–100 kV cold FEG with 0.3 eV native energy spread, and a high-energy-resolution monochromator capable of delivering 5 meV energy resolution. For EELS analyses, a Nion IRIS high-energy-resolution EELS spectrometer with Dectris ELA

direct electron detector was used. EEL spectra were acquired using low beam currents < 3 pA (adjusted by closing the monochromator slit width, resulting in an effective energy resolution of 60 meV) to avoid damage of fragile organic material. Data was collected in STEM mode with a rastered beam. EELS maps were obtained by integrating the intensity above the various ionization edges over suitable energy windows after removal of the background using a standard power-law model. Quantification was carried out using the model-based approach initially developed by Verbeeck et al. (2006) and implemented in Gatan's GMS3.5 software suite (Gatan Ametek Inc., Pleasanton, USA), relying on tabulated Hartree-Slater cross-sections. Thanks to the ELA detector's high dynamic range, all spectra were recorded over an extended energy range including the zero-loss peak, enabling plural scattering removal and precise energy calibration as part of the quantification procedure, and thus enabling the creating of quantitative areal density maps rather than relative spectral intensity maps.

2.3. NanoSIMS measurements of carbon and nitrogen isotopes

Carbon and nitrogen isotopic compositions were analyzed on a Cameca NanoSIMS 50 at the Max Planck Institute for Chemistry in Mainz. Isotopic measurements were performed using a ~ 1 pA Cs^+ primary ion beam with a beam size of about 100 nm. Isotopes were measured as negative secondary ions in multi-collection mode ($^{12}\text{C}^-$, $^{13}\text{C}^-$, $^{12}\text{C}^{14}\text{N}^-$, $^{12}\text{C}^{15}\text{N}^-$ and $^{28}\text{Si}^-$). Mass resolution was sufficient ($m/\Delta m > 8000$, CAMECA-definition, using a 15–85 % slope, at mass 26) to clearly separate $^{13}\text{C}^-$ from $^{12}\text{C}^{14}\text{H}^-$, and $^{12}\text{C}^{15}\text{N}^-$ from $^{13}\text{C}^{14}\text{N}^-$, and to exclude contributions from the tail of the $^{11}\text{B}^{16}\text{O}^-$ peak to $^{12}\text{C}^{15}\text{N}^-$. The ion counting rates of $^{12}\text{C}^-$ and $^{12}\text{C}^{14}\text{N}^-$ were corrected for quasi-simultaneous arrivals (QSA) with correction factors according to Slodzion et al. (2004) and Hillion et al. (2008). Corrections were applied individually for each grain or region of interest. Carbon and nitrogen isotopic ratios were normalized to those measured on a synthetic N-doped SiC standard with a known composition of $\delta^{13}\text{C}_{\text{PDB}} = -29$ ‰ ($^{13}\text{C}/^{12}\text{C}_{\text{PDB}} = 0.011237$) and terrestrial $^{15}\text{N}/^{14}\text{N}$ ($^{15}\text{N}/^{14}\text{N}_{\text{air}} = 3.676 \times 10^{-3}$). Deviations of the isotopic compositions from the respective standard ratios are reported as δ -values, displaying the deviation in per mil:

$$\delta(^A E/^B E) = \left\{ \left[\frac{(^A E/^B E)_{\text{meas}}}{(^A E/^B E)_{\text{std}}} - 1 \right] \right\} \times 1000$$

with $^A E/^B E$ being the ratio of two isotopes of a given element E with mass numbers A and B. Prior to analysis, selected areas were sputter-cleaned with a higher current Cs^+ beam (~ 20 pA) to remove contamination and to implant primary ions. Isotope distribution in particles was visualized by ion images. Each image consists of 5 scan layers that were added together, each lasting about 11 min for 256×256 pixels (whole analysis time: 55 min per section). Combination of different image layers allows correction for image shifts during analysis resulting in improved counting statistics. Data was processed using a custom software developed at by the Max Planck Institute for Chemistry in Mainz.

3. Results

3.1. Texture and Petrography

Although all particles investigated are assigned to the chondritic-porous subset, they exhibit major textural differences. The main phases found in the analyzed IDPs are GEMS, Mg-rich crystalline silicates, Fe-(Ni)-sulfides, Fe-metal, and carbonaceous material. While particles L2099 A7 and L2099 A8 appear mostly fine-grained and compact with crystalline silicate phases of 100–500 nm size, particles L2083 E51, L2083 B1, and L2071 AB1 are highly porous, exhibit a greater fraction of GEMS and other distinct crystals of few μ m in size. The different microstructures of the particles will be described in detail in the following sections.

3.1.1. Textural description of GEMS

In this study, we explicitly focus on the amorphous Mg-silicate glass in GEMS acting as matrix for the nanophase inclusions of Fe-Ni-metal and Fe-sulfides, because amorphous silicates are of enormous importance in many astrophysical environments such as the interstellar medium (ISM) or as amorphous silicate material in primitive meteorites (Abreu, 2016; Abreu and Brearley, 2010; Dobrică and Brearley, 2020; Hopp and Vollmer, 2018; Greshake, 1997; Le Guillou et al., 2015;

Leroux et al., 2015; McAdam et al., 2018; Ohtaki et al., 2021; Vollmer et al., 2020). In the investigated particles, GEMS constitute up to 40 vol % of total particle volume and the abundances and sizes of GEMS and their inclusions vary strongly. Particles L2099 A7 and L2099 A8 display a fine-grained texture and contain no clearly defined GEMS. Areas with similarities to GEMS are hallmarked by very small sulfide and metal inclusions of only a few nanometers in diameter, causing the fine-grained texture of the particles (Fig. 1a). Moreover, magnetite rims

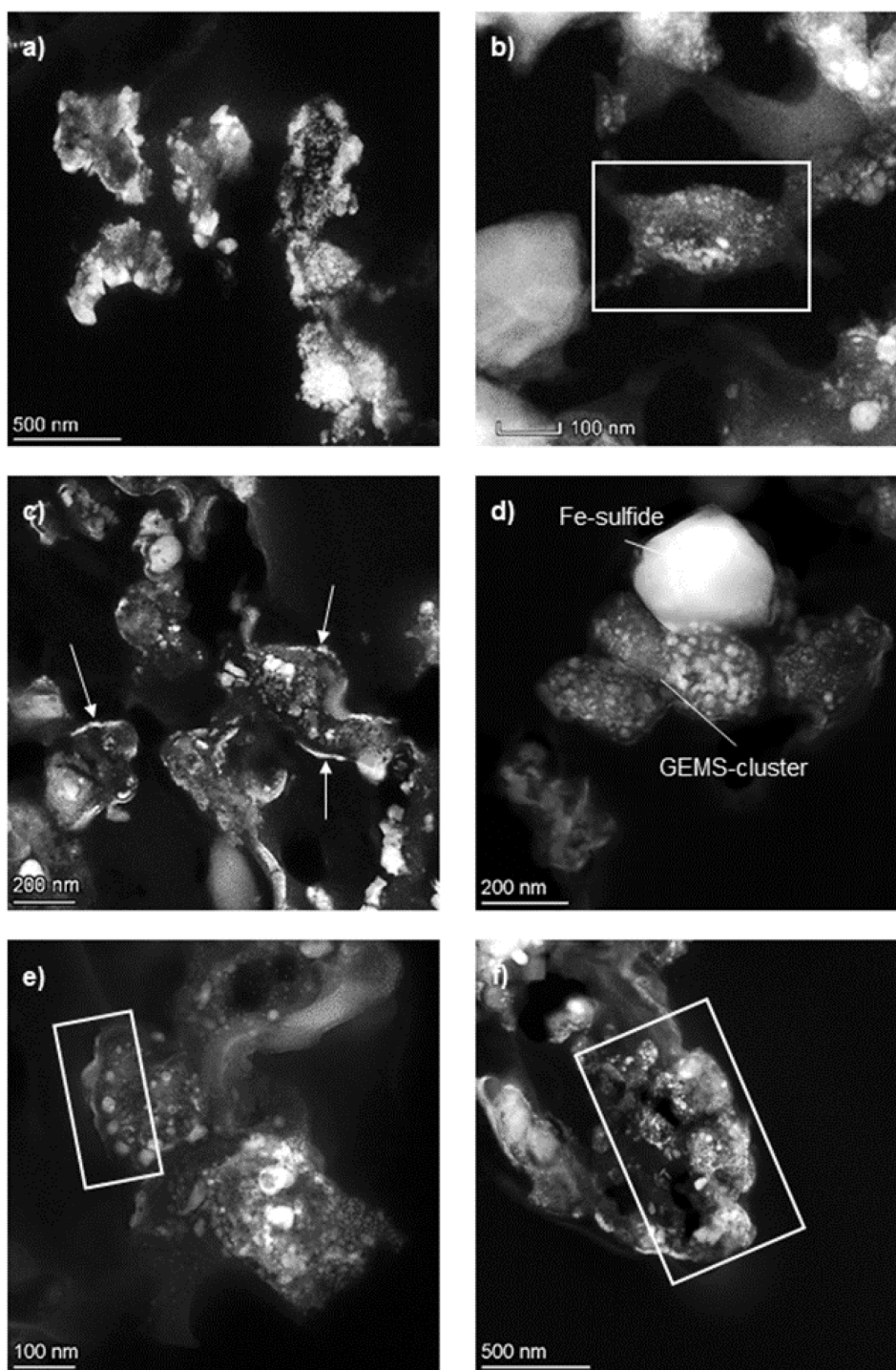


Fig. 1. HAADF images of the different styles of GEMS found in the investigated particles: a) fine-grained fluffy GEMS area in particle L2099 A8; b) single aggregate GEMS in the middle of particle L2083 E51; c) magnetite rims (white arrows) on GEMS in particle L2083 E51; d) cluster of 3 individual GEMS attached to a sulfide grain in particle L2071 AB1; e) GEMS with inclusions aligned at the rim of particle L2083 E51 (white box) and next to a second GEMS with different sized inclusions inside; f) GEMS-like area in particle L2083 E51 with individual GEMS grains not clearly identifiable (white box).

cover these areas. The GEMS areas with very fine inclusions also have less observable amorphous silicates. In all other particles investigated, GEMS appear more distinct and as discrete phases. They are mostly rounded, often oval, with sizes between 300 and 400 nm in diameter but can also occur as smaller grains of only 100 nm in size (Fig. 1b). GEMS on the exteriors of the IDPs can have magnetite rims of a few nanometers thickness (Fig. 1c). GEMS mostly do not occur as isolated phases but form clusters of two or more GEMS attached to each other (Fig. 1d). Abundances and sizes of Fe-Ni-metal and Fe-sulfide inclusions vary. Although most inclusions of a single GEMS have the same size (mostly a few nanometers), some GEMS have one large inclusion and several smaller ones unequally distributed throughout the grain (Fig. 1e). Some GEMS show textures with inclusions aligned on the grains' rims (Fig. 1e). GEMS connected in a cluster do not necessarily have the same textural appearance. The abundance of inclusions as well as the sizes of inclusions varies between discrete GEMS in a GEMS cluster. In some GEMS clusters, boundaries of individual GEMS as small as 20 nm are not directly observable, but slightly different morphologies suggest the existence of several smaller grains (Fig. 1f). The subgrains can also be distinguished by elemental maps, especially of Mg, because of compositional heterogeneities. Distinct single GEMS are rare in all investigated particles. They occur only in the interior of the IDPs (Fig. 1b) and are very small (100–200 nm in diameter). Otherwise, they do not differ from GEMS in clusters. They also have inclusions with variable sizes which can be equally or unequally distributed throughout the grain.

3.1.2. Mineralogy of crystalline grains in IDPs

Crystalline grains appear in different forms in the investigated particles. In particles L2099 A7 and L2099 A8 they are mostly found in the form of polycrystalline aggregates (Fig. 2a). The individual subgrains have sizes between a few nm (as in L2099 A8) up to 200 nm (in L2099 A7) and are irregularly shaped. The polyphase grains are arranged in clusters of 1–2 μm size. In the two aforementioned particles they make up almost the complete volume of the particles, while they are almost absent in particles L2083 B1, L2083 E51, and L2071 AB1. Mineralogy of the individual subgrains is difficult to distinguish because of the small grain sizes and the close associations between individual crystals. They mostly resemble the so-called equilibrated aggregates (EAs) (Bradley, 1994) and will be described as such in the following. Nevertheless, from elemental maps and handpicked EDX area quantification, mostly Mg-rich silicate minerals (enstatite and forsterite) were identified in EAs, as well as minor Fe-sulfide crystals. The sulfides are smaller than the silicate minerals in EAs (20–50 nm). EAs on the edges of particles in L2099 A7 and A8 are often decorated with magnetite rims. When magnetite rims are observed around EAs, they do not contain any sulfides as subgrains. The more EAs a particle contains, the less GEMS are observed. Sometimes EA areas mimic textures of GEMS grains, as they are rounded and contain crystallites of a few nm clustered together.

Besides as EAs, crystalline silicates also occur as discrete individual grains in the investigated particles with euhedral, elongated morphologies. They are mostly larger than the EAs (between 500 nm and 2 μm), only in particle L2099 A1a Mg-silicates of around 200 nm length occur. In particle L2083 E51 silicate minerals are about 1–2 μm in length and on average 200 nm in width (Fig. 2b). They make up to 21 % of total particle volume. EAs are completely absent in L2083 E51. A similar elongated enstatite crystal is also found in L2083 B1, but here it is a single isolated grain with a size of $0.5 \times 1.5 \mu\text{m}$. Where the single crystal adjoins the particle rim, it is surrounded by a rim structure of fine-grained material. The EDX maps of the elongated crystals show, that they are overall Mg-rich, but have slightly elevated Fe-contents to the rims, while the interior is more Mg-rich. It is noteworthy that all euhedral enstatite crystals are found towards rims of particles, never completely in the interior.

Furthermore, crystalline silicates also occur as irregular or rounded isolated crystals of 50–200 nm in size (Fig. 2c). This type is mostly found in the interior of particles and EDX maps show that they are chemically homogeneous and Mg-rich. They are similar to EAs, but clearly represent single mineral phases in contrast to polymineralic EAs. They make up only a few vol% of some particles.

While the previously mentioned crystalline silicate minerals are all Mg-rich and can therefore either be identified as enstatite or forsterite grains, particle L2076 B5 contains a large ($1 \times 1 \mu\text{m}$) silicate grain rich in Ca identified as diopside. It is shattered due to particle preparation via ultramicrotomy.

Other prominent isolated grains found in the analyzed particles are sulfides, Fe-oxide and Na-Al-rich grains. Sulfides are found in almost all particles as discrete grains of various sizes. A euhedral sulfide grain with a pentagonal shape is found in particle L2071 AB1. It is ~ 200 nm in diameter and has a detached rim, possibly from ultramicrotome preparation (Fig. 3a). Other individual sulfide grains in the investigated particles are much smaller, mostly up to 50 nm and rounded. In particle L2099 A1a, a single magnetite grain is found. It is 540×310 nm in size and has a rectangular shape, next to an oval troilite of 250×180 nm in size (Fig. 3b). Another isolated grain is only found in particle L2076 B5 next to the diopside grain described above. This phase is irregularly shaped and rich in Na and Al, but no definite mineral phase can be assigned based on its stoichiometry (Fig. 3c).

3.2. Chemical composition

3.2.1. Chemical composition of bulk interplanetary dust particles

A total of 18 sections of eight IDPs was mapped, and three sections of the CI meteorite Orgueil using the same analysis parameters to obtain chemical composition of bulk particles as well as of different mineral phases.

All IDPs contain carbon, however, quantification is not possible,

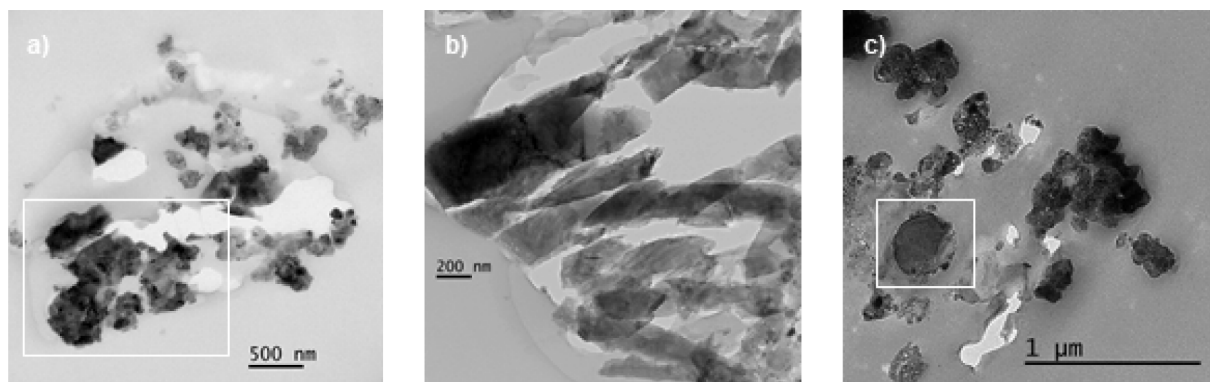


Fig. 2. Different textures of crystalline silicate minerals in the investigated IDPs: a) equilibrated aggregates in particle L2099 A7 (white square); b) elongated Mg-silicate crystals in L2083 E51; c) perfectly rounded Mg-silicate grain in particle L2099 A7 (white square).

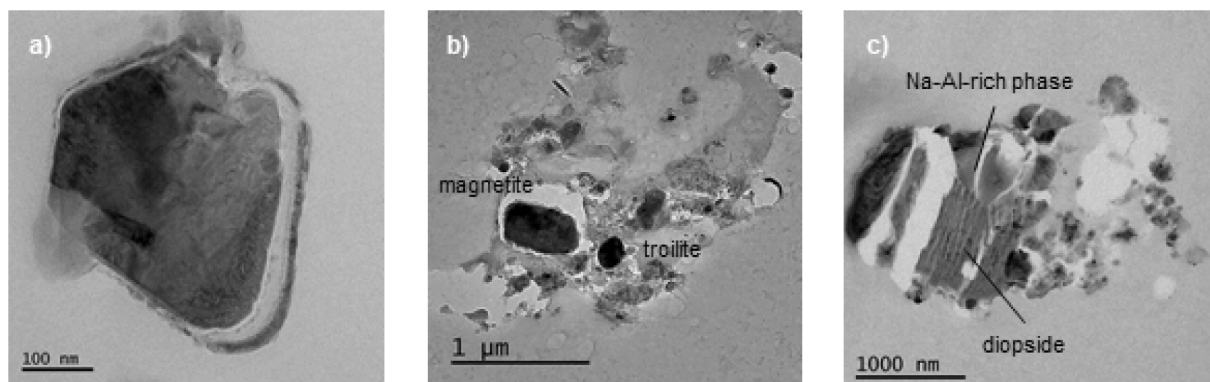


Fig. 3. Types of isolated grains found in investigated IDPs: a) euhedral sulfide with detached rim, possibly from ultramicrotome preparation, in particle L2071 AB1; b) prominent magnetite and troilite grains in L2099 A1a; c) Na-Al-rich phase next to the shattered diopside in particle L2076 B5.

because of the amorphous carbon support film and the epoxy that contribute to analyses. Nevertheless, indigenous carbon is identified in qualitative EDX maps by slightly different contrast and the fact that it is often associated with nitrogen, which is absent in the carbon film and the epoxy (Fig. S2, supplementary material). Contents of most other major elements vary by up to two orders of magnitude (Table 1). All particles (on average) are subsolar for Mg/Si, S/Si, Fe/Si (except L2099 A1a Grid2 Sec04), and Ni/Si. L2076 B5, which contains Ca-Mg-silicates and Na- and Al-rich phases, is consequently enriched in Ca/Si and Al/Si compared to all other particles. L2099 A1a Grid2 Sec04 is richer in Fe/Si than any other section by a factor of 2.8. This section is dominated by a large euhedral magnetite grain and a Fe-sulfide. In addition to that, crystalline Mg-silicates (mostly of enstatite composition) in this section appear intermixed with Fe on the nanoscale in the elemental maps.

Table 1

Element/Si ratios of 8 bulk interplanetary dust particles, 5 sections of CI chondrite Orgueil, solar value and bulk IDP data from the literature; absolute errors are 1 σ range.

	Mg/Si	Al/Si	S/Si	Ca/Si	Fe/Si	Ni/Si
L2099 A1a (n = 2)	0.42 ± 0.05	0.12 ± 0.01	0.36 ± 0.07	0.13 ± 0.01	1.02 ± 0.67	0.03 ± 0.01
L2099 A7 (n = 1)	0.63 ± 0.20	0.02 ± 0.01	0.05 ± 0.01	0.06 ± 0.02	0.38 ± 0.10	0.02 ± 0.01
L2099 A8 (n = 2)	0.33 ± 0.08	0.06 ± 0.02	0.05 ± 0.01	0.29 ± 0.00	0.41 ± 0.11	0.03 ± 0.01
L2071 AB1 (n = 2)	0.24 ± 0.01	0.03 ± 0.03	0.18 ± 0.01	0.02 ± 0.00	0.23 ± 0.01	0.01 ± 0.00
L2083 B1 (n = 3)	0.47 ± 0.07	0.02 ± 0.02	0.08 ± 0.02	0.01 ± 0.00	0.25 ± 0.03	0.01 ± 0.00
L2076 B5 (n = 3)	0.64 ± 0.08	0.15 ± 0.01	0.11 ± 0.04	0.18 ± 0.06	0.26 ± 0.12	0.01 ± 0.00
U2153 B4 (n = 2)	0.55 ± 0.05	0.04 ± 0.01	0.07 ± 0.00	0.03 ± 0.00	0.36 ± 0.04	0.02 ± 0.00
L2083 E51 (n = 3)	0.28 ± 0.16	0.04 ± 0.02	0.05 ± 0.01	0.01 ± 0.01	0.19 ± 0.02	0.00 ± 0.00
Average all IDP samples (n = 18)	0.44 ± 0.05	0.06 ± 0.01	0.12 ± 0.03	0.06 ± 0.02	0.36 ± 0.08	0.01 ± 0.00
Orgueil (n = 5)	0.83 ± 0.05	0.11 ± 0.00	0.03 ± 0.00	0.09 ± 0.02	0.36 ± 0.05	0.03 ± 0.01
Solar abundances based on CI (Palme et al., 2014)	1.03	0.08	0.44	0.06	0.88	0.05
Average of 90 bulk CP-IDPs (Schramm et al., 1989)	1.015	0.07	0.417	0.047	0.705	0.024
Bulk IDP U2- 20B11 (from Bradley et al., 1984)	0.959	0.064	0.54	0.045	0.656	0.027

Oxidized areas with elevated Fe have similarities with GEMS but contain too little S and Ni in inclusions to be identified as true GEMS. All these phases might account for the overall higher Fe/Si in this section. Orgueil is classified as a CI chondrite and its chemical composition is closest to solar abundances (Asplund et al., 2021). Our Orgueil analyses match the solar abundances within 2 σ , therefore, we conclude that using the same measurement parameters for IDP analyses obtains robust results.

Most of the euhedral crystalline silicates in the analyzed IDPs are Mg-rich with a mean Mg-content of 17.3 at%. This is a bit lower than Mg-content of 18.6 at% of a pyroxene crystal in IDP W7028 C4 reported by Bradley (1994). Although the majority of analyses point to a pyroxene stoichiometry (and minor olivine), some extend to Si-enriched values. The extension to Si-rich compositions is more pronounced for the more xenomorphic crystals as well as the EAs.

Sulfide compositions inside investigated IDPs vary with the amount of Ni incorporated. Most sulfides are stoichiometric troilite (FeS) (n = 15) or pyrrhotite (Fe_{1-x}S) (n = 31) with a maximum Ni-content of 4 at% Ni. Ni-rich pentlandite, which is a common sulfur-bearing mineral in hydrous IDPs and carbonaceous chondrites, was not detected in any of the IDPs in this study.

3.2.2. Chemical composition of GEMS amorphous silicates

A total of 105 Regions of Interest (ROIs) inside GEMS grains was analyzed. Except for one GEMS in particle L2083 E51, where 7 ROIs were measured in the same GEMS aggregate grain, a ROI always corresponds to the amorphous silicates of one aggregate GEMS grain or a distinct GEMS-like area. Table 2 shows the major element composition of the amorphous silicates inside 105 ROIs in GEMS relative to Si compared to previous measurements of GEMS amorphous silicates as well as bulk GEMS compositions taken from the literature, and the solar abundance of elements. In bulk GEMS measurements, the nanophase inclusions of Fe-Ni-metal and Fe-sulfide are included, so that the complete grains are analyzed. Mg/Si values of the GEMS amorphous silicates range between 0.01 and 1.34, therefore vary by two orders of magnitude. The average Mg/Si is 0.43 ± 0.03, which is slightly lower than the average of 0.67 for bulk GEMS grains reported by Keller and Messenger (2011) and the value of 0.65 for bulk GEMS taken from Ishii et al. (2018). It is also lower than the average for GEMS amorphous silicates of 0.91 reported by Ohtaki et al. (2021). Average Mg/Si of our analyses is also lower than the solar value of 1.03. Iron content of the GEMS amorphous silicates shows the same variability. The average Fe/Si of GEMS amorphous silicates in all six particles is 0.20 ± 0.02 but ranges from 0.02 to 0.93. The solar Fe/Si is 0.85, therefore, most of the GEMS amorphous silicates analyses are subsolar for Fe/Si. Furthermore, bulk GEMS measurements by Bradley (1994), Ishii et al. (2008), and Keller and Messenger (2011) display higher Fe/Si values than in this study. Compared to GEMS amorphous silicates measured by Ohtaki et al. (2021), GEMS amorphous silicates in this study exhibit nearly one order

Table 2

Major element composition of GEMS amorphous silicates in particles L2099 A7, L2099 A8, L2071 AB1, L2083 B1, L2076 B5, and L2083 E51 compared to bulk GEMS compositions, solar abundance of the elements, and the composition of amorphous silicate material in the primitive CI-chondrite Acfer 094.

	Mg/Si	Al/Si	S/Si	Ca/Si	Fe/Si	Ni/Si
Average of 105 GEMS amorphous silicates analyses	0.43 ± 0.03	0.05 ± 0.00	0.04 ± 0.00	0.02 ± 0.00	0.20 ± 0.02	0.01 ± 0.00
Range	0.01–1.34	0.0012–0.14	0–0.09	0–0.1	0.02–0.93	0–0.05
L2099 A7 (n = 10)	0.76 ± 0.08	0.05 ± 0.00	0.02 ± 0.01	0.02 ± 0.00	0.20 ± 0.01	0.02 ± 0.00
Range	0.49–1.28	0.029–0.077	0.0079–0.06	0.005–0.04	0.14–0.27	0.01–0.03
L2099 A8 (n = 8)	0.35 ± 0.13	0.05 ± 0.00	0.02 ± 0.01	0.01 ± 0.00	0.23 ± 0.10	0.02 ± 0.00
Range	0.09–1.22	0.034–0.066	0–0.058	0.002–0.03	0.079–0.93	0.005–0.03
L2071 AB1 (n = 18)	0.26 ± 0.05	0.07 ± 0.00	0.05 ± 0.00	0.01 ± 0.00	0.22 ± 0.04	0.01 ± 0.00
Range	0.0422–0.79	0.037–0.14	0.021–0.086	0.001–0.06	0.033–0.73	0.003–0.05
L2083 B1 (n = 16)	0.62 ± 0.05	0.04 ± 0.003	0.05 ± 0.00	0.02 ± 0.00	0.18 ± 0.03	0.01 ± 0.00
Range	0.285–0.921	0.001–0.09	0–0.88	0.008–0.03	0.032–0.46	0.003–0.02
L2076 B5 (n = 2)	0.72 ± 0.05	0.07 ± 0.01	0.04 ± 0.00	0.04 ± 0.00	0.27 ± 0.01	0.01 ± 0.00
Range	0.571–0.863	0.036–0.095	0.015–0.066	0.04–0.04	0.24–0.3	0–0.02
L2083 E51 (n = 50)	0.36 ± 0.05	0.05 ± 0.00	0.05 ± 0.00	0.02 ± 0.00	0.19 ± 0.03	0.01 ± 0.00
Range	0.011–1.34	0.0032–0.14	0.0022–0.09	0–0.1	0.023–0.69	0–0.04
Bulk GEMS (n = 42) (Ishii et al., 2008)	0.65	0.11	0.27	0.06	0.44	0.03
Bulk GEMS (n = 3) (Bradley, 1994)	0.638	0.0395	0.222	0	0.363	0.00601
Bulk GEMS (n = 239) (Keller & Messenger, 2011)	0.67	0.07	0.3	0.04	0.56	0.03
Range	0.05–1.44	0–0.21	0.01–1.25	0–0.23	0.96–1.63	0–0.12
GEMS amorphous silicates (Ohtaki et al., 2021)	0.91 ± 0.36	0.08 ± 0.03	0.09 ± 0.11	0.03 ± 0.02	0.15 ± 0.12	0.01 ± 0.01
Bulk GEMS (Ohtaki et al., 2021)	0.61 ± 0.28	0.10 ± 0.04	0.25 ± 0.20	0.04 ± 0.04	0.43 ± 0.30	0.03 ± 0.03
solar value (Palme et al., 2014)	1.03	0.09	0.42	0.06	0.85	0.05

of magnitude higher Fe/Si but still lower than bulk GEMS. Compositional trends are also shown in the Mg-Si-Fe ternary diagram in Fig. 4.

Fig. 4 shows that no systematic compositional trends are observed in particles, where GEMS from more than one grid have been investigated. There are especially no trends from earlier- to later-sliced grids, inferring no compositional zoning from core to rim in individual GEMS grains.

Nearly all GEMS grains are identified as clusters of several subgrains stuck together. They can be distinguished by small variations in Mg- and Si-content in each subgrain in the EDX elemental maps. Fig. 5 shows an example of two adjacent GEMS aggregate grains in particle L2083 E51 Gr3 Sec01. The Mg-Si-elemental map shows that the two GEMS consist of several domains with variable Mg-content, with the smallest domains being around 45 nm in diameter (Fig. 5b). In some cases, carbon surrounds individual GEMS subgrains and correlates with Mg-poor and Si-rich regions. Between the two aggregate GEMS grains, X-ray intensities

of carbon are higher around the subgrains, compared to the carbonaceous material diffusely distributed throughout the particle. Moreover, the left GEMS aggregate shows a complex rim texture on the lower left part, with a double carbon rim and Mg-Si-rich matter between the two carbon layers. We observe this texture on some of the smallest GEMS aggregate grains in the interiors of the particles, and not the particle edges.

Carbon rim structures are especially found around GEMS grains in the particles, that have been identified as less altered by the absence of recrystallized EA material and no or very thin magnetite rims. Fig. 6 shows an EELS carbon areal density map of a GEMS cluster area in particle L2071 AB1 Grid3 Sec02. The areal density means atoms per unit area and can therefore be taken as an indicator for density differences. The lower part of the map area corresponds to the carbonaceous matrix material with two Fe-sulfide grains embedded. This carbonaceous matter has a clearly different contrast than the material between individual

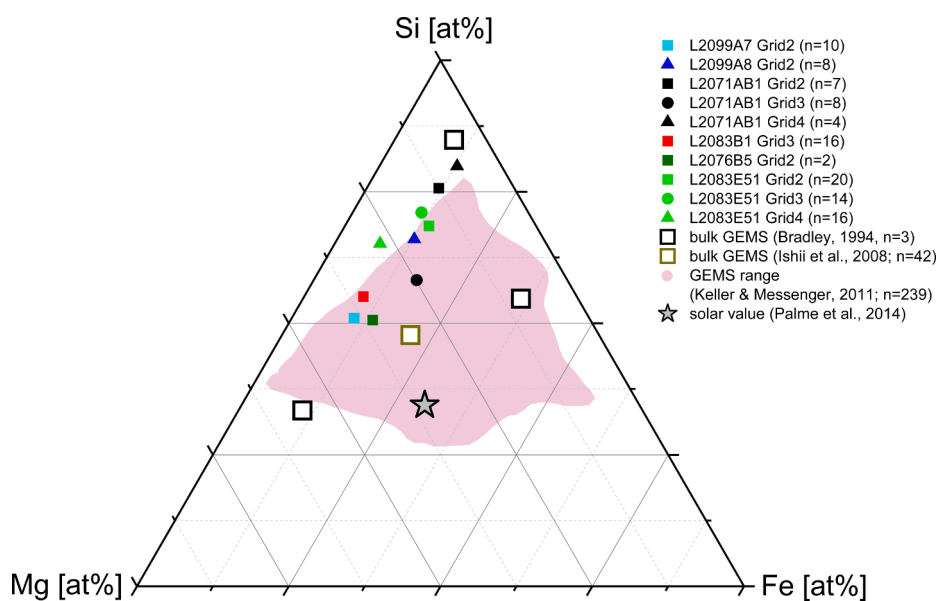


Fig. 4. Mean grid compositions of GEMS amorphous silicates (Table 2) of particles L2099 A7, L2099 A8, L2071 AB1, L2083 B1, L2076 B5, and L2083 E51 plotted in a Mg-Si-Fe ternary diagram, compared to bulk GEMS measurements taken from the literature (open squares, pink shaded area) and the solar value (grey star, taken from Palme et al. (2014)).

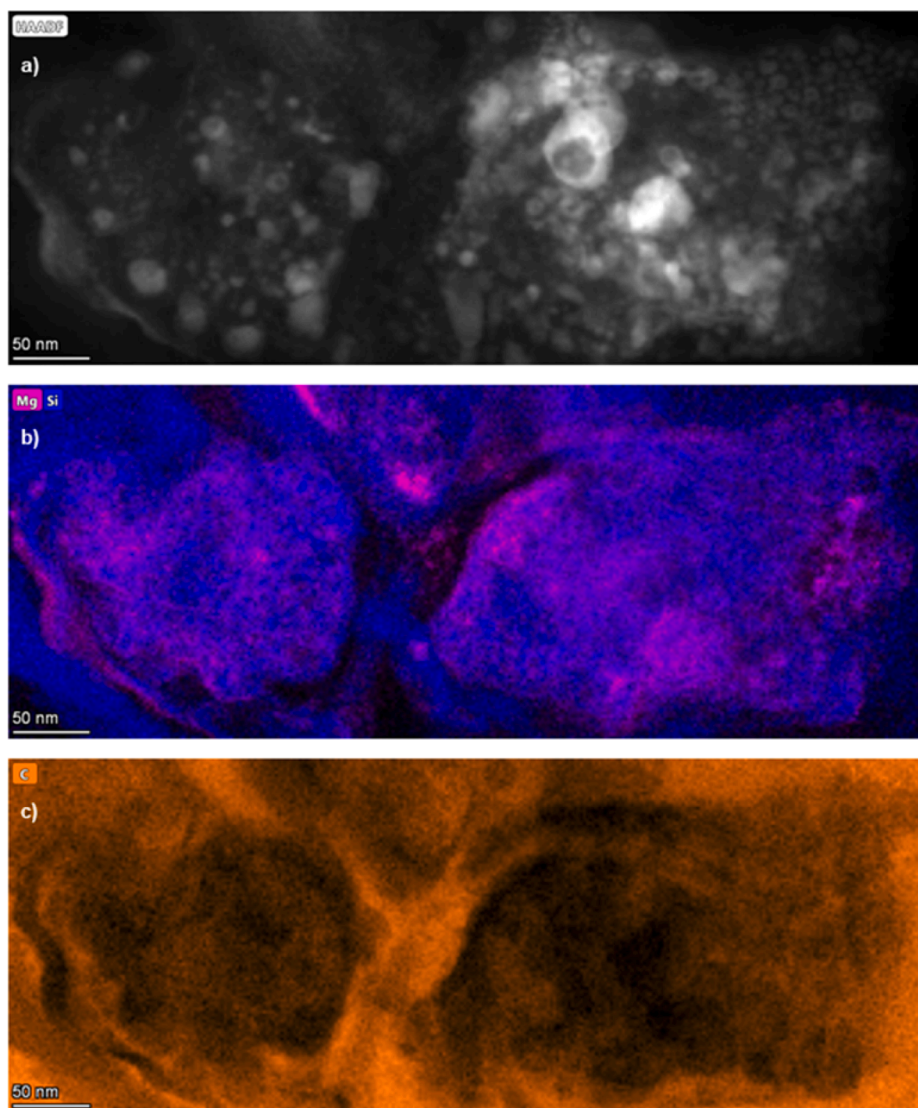


Fig. 5. a) HAADF image of two neighboring GEMS grains in particle L2083 E51 Gr3 Sec01; b) Mg (purple) and Si (blue) elemental map of the GEMS grains showing different domains with varying Mg-content, interpreted as subgrains inside the GEMS grains; c) corresponding C elemental map (orange) showing the carbon content roughly correlated with coating on GEMS subgrains. Furthermore, there seems to be a higher-density area in the contact zone between the two GEMS as shown by the brighter X-ray contrast and a rim structure to the outside of the GEMS aggregate grains.

GEMS subgrains in the GEMS cluster in the upper part of the map area. The carbon around GEMS subgrains in the GEMS cluster has an areal density of around 6000 atoms/nm², while the carbonaceous matrix material has only 3100 atoms/nm². A very bright spot in the EELS carbon areal density map directly located to the lower edge of the GEMS cluster might correspond to a possible carbon nanoglobule. This structure has even 7800 atoms/nm². Furthermore, the areal density of silicon atoms is low inside the GEMS cluster, but remarkably higher around it and in the IDP matrix (Fig. 6c).

S/Si of the amorphous silicates in GEMS in this study varies between 0 and 0.09 with an average of 0.04. GEMS amorphous silicates in our particles are subsolar for S/Si (solar S/Si is 0.42), but some extend to slightly higher values. Fe is not always coupled to S in GEMS as some analyses display high iron contents but almost no S. Besides Mg, Si, and Fe, the matrix contains small amounts of Ca and Al as well. The average Ca/Si of all particles is 0.02 with the maximum value of Ca/Si (0.1) in particle L2083 E51. Compared to the solar value (0.06), all investigated particles are depleted in Ca on average, although higher values occur.

To conclude, our measurements show that GEMS amorphous silicates are subsolar for almost all major element/Si ratios. There are

variations among Mg- and Fe-contents observable, but all amorphous silicates range from enstatite compositions to very Si-enriched compositions. In contrast to previous bulk GEMS measurements, the GEMS amorphous silicates are depleted in Fe.

3.3. Carbon and nitrogen isotopic composition of organic matter

The isotopic composition of organic matter surrounding GEMS and other IDP components as matrix material or encapsulating GEMS themselves, can give additional hints on formation conditions of the particles and their components. In Fig. 7, the $\delta^{15}\text{N}$ values are plotted against the $\delta^{13}\text{C}$ of the investigated sections. All investigated sections (except for L2083 B1 Grid3 Sec07 which is close to the terrestrial value) are enriched in ¹⁵N by ~ 100 ‰ on average compared to the terrestrial value. This is comparable to bulk nitrogen isotopic compositions of IDPs with positive $\delta^{15}\text{N}$ values of several hundred ‰ up to 1300 ‰ (Chan et al., 2020; Floss et al., 2004; Floss et al., 2006). Compared to various carbonaceous chondrite groups, the IDPs mostly show heavier nitrogen isotopic compositions. CR2 chondrites are typically the most enriched with $\delta^{15}\text{N}$ ~ 150 ‰ and decreasing values with increasing petrologic

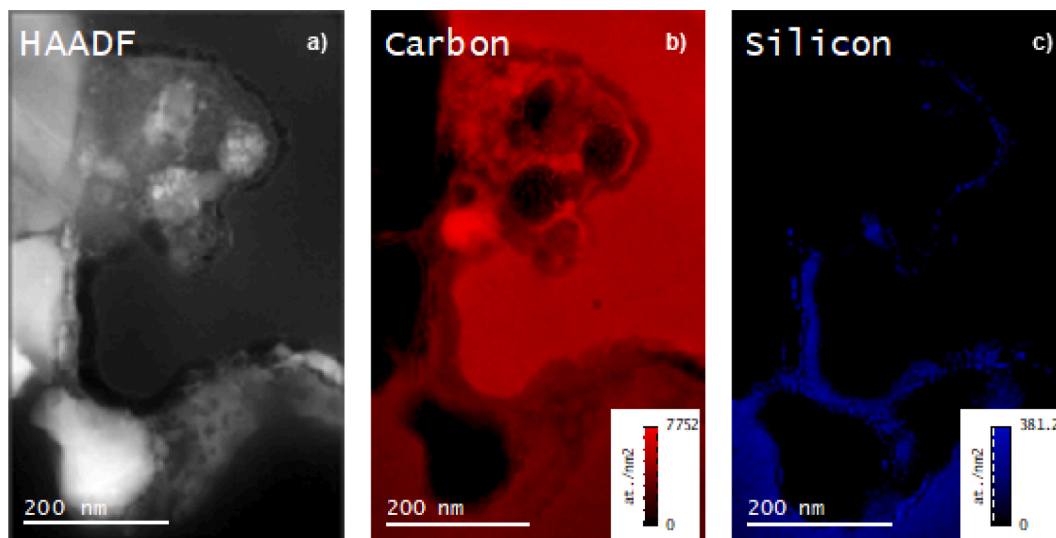


Fig. 6. a) HAADF image of a GEMS cluster area in particle L2071 AB1 Grid3 Sec02; b) corresponding EELS carbon areal density map (atoms/nm²). Carbon between small GEMS subgrains in the GEMS cluster has higher areal density than the one to the lower part of the area, where carbonaceous matrix material is located; c) corresponding EELS silicon areal density map showing the contamination of sensitive carbonaceous matrix material with silicon, possibly silicon oil contamination. Furthermore, the silicon clusters around the outer shape of the GEMS cluster in the upper part of the map but does not penetrate the grains. Therefore, silicon oil contamination of GEMS can be excluded.

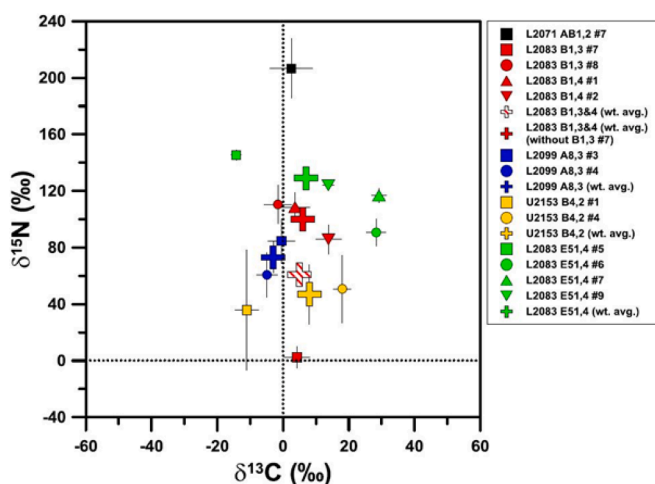


Fig. 7. Average carbon and nitrogen isotopic composition of organic matter in investigated sections of particles L2071 AB1, L2083 B1, L2099 A8, U2153 B4, and L2083 E51. Dashed lines represent the terrestrial values. All errors are 1σ .

type (Pearson et al., 2006).

The carbon isotopic composition, in contrast to nitrogen, clusters around the terrestrial value with a slight enrichment in ¹³C of around 20 ‰ which is also comparable to previous IDP compositions with $\delta^{13}\text{C} = -100$ to $+163$ ‰ (Floss et al., 2006). Furthermore, different sections of the same particle show some variability in $\delta^{15}\text{N}$ and $\delta^{13}\text{C}$. Sections of particle L2083 B1 and L2083 E51 show a negative correlation of carbon and nitrogen isotopic compositions with higher $\delta^{13}\text{C}$ values correlating with lower $\delta^{15}\text{N}$ values. For particles L2099 A8 and U2153 B4, sections with higher $\delta^{13}\text{C}$ values have also higher $\delta^{15}\text{N}$ values, although the error in the nitrogen isotopic composition is larger in these sections. The highest enrichment in ¹⁵N is observed in L2071 AB1 Grid2 Sec07, but this bulk particle enrichment is profoundly affected by one discrete “hotspot” that shows an extreme $\delta^{15}\text{N}$ value of 1177 ± 86 ‰. The hotspot is one of three N-bearing sub-regions in this section, but the one with the most extreme $\delta^{15}\text{N}$ composition. The other two analyses are -10 and $+120$ ‰, respectively.

Carriers of the isotopic anomalies might be identified in STEM-HAADF and BF images. However, this was not possible for all sections because those taken for NanoSIMS analysis were mostly located on grid bars of the Cu-TEM-grids. Hence, neighboring sections were investigated to locate regions of isotopic anomalies, although particles might appear different in neighboring sections as described above.

Fig. 8a shows, that the anomalous region in L2071 AB1 consists of different phases like silicates, sulfides, and some GEMS-like phases as well as carbonaceous material distinguishable by the light grey haze in the HAADF image. The carbonaceous material is diffusely distributed over this area and is most likely the carrier of the isotopic anomaly. A specific organic phase like an organic globule is not clearly identifiable in this area. In particle L2083 E51 Grid4 Sec05, several nitrogen isotopic measurements show positive $\delta^{15}\text{N}$ values of about 200–600 ‰. The HAADF image of that area (Fig. 8b) is dominated by a low-Z material in a haze-like texture, which is most likely carbonaceous material. The carbonaceous material fills an interstice of about 1 μm in diameter within the particle and is surrounded by small GEMS and Mg-silicate grains connecting the other IDP parts. Therefore, the main carrier of isotopic anomalies in this particle as well as in the previous described particle L2071 AB1 Grid2 Sec07 is carbonaceous material with variable amounts of nitrogen (up to 8 at% measured by EDX).

It is not possible to completely avoid the inclusion of the carbon film of the TEM grids or the epoxy during isotopic analysis, because particles are highly porous and the field of view of the NanoSIMS is always a bit larger than the particle size. In EDX maps of the particles, the regions with the organic matter do contain nitrogen in contrast to the epoxy and the carbon film (Fig. S2, supplementary material). Therefore, only sections with adequate carbonaceous matrix material between components were chosen for isotopic analyses.

4. Discussion

4.1. Differentiation between primary and secondary features in anhydrous IDPs

4.1.1. Atmospheric entry heating

All investigated IDPs are assigned to the chondritic-porous subset and are thought to originate from comets from the outer solar system. Therefore, aqueous alteration on the parent body is limited due to the

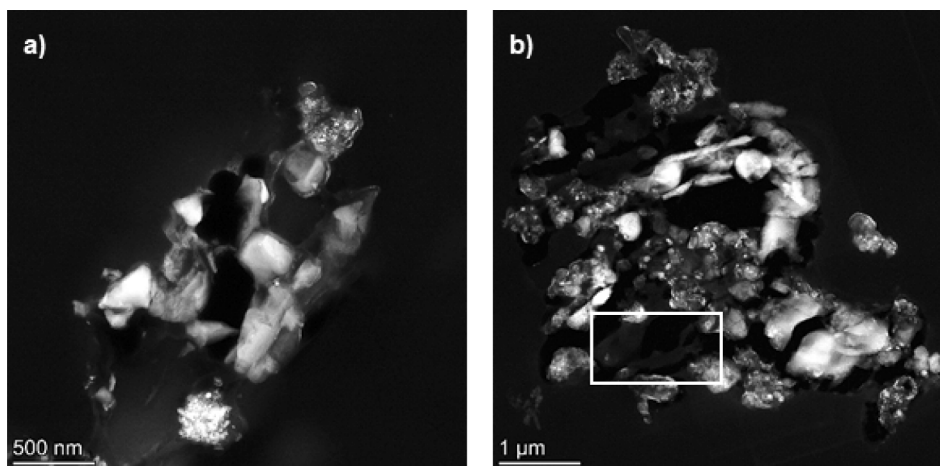


Fig. 8. a) STEM-HAADF image of the area with the high $\delta^{15}\text{N}$ value of 1177 ‰ in particle L2071 AB1 Grid2 Sec10; b) STEM-HAADF image of particle L2083 E51 Grid4 Sec04 with the area indicated, in which higher positive $\delta^{15}\text{N}$ values were measured.

requirement of very specific conditions to retain liquid water on the comet (Nakamura-Messenger et al., 2011).

IDPs can also be altered by other mechanisms such as heating during atmospheric entry. After release from their parent body, particles spiral inwards in the solar system because of Poynting-Robertson drag (Flynn, 1990). They then enter the upper atmosphere, decelerate, and descend into the stratosphere, where they are concentrated, and can be collected by NASA high-altitude aircrafts with special collector surfaces. Depending on their sources and orbits, particles enter the stratosphere at different angles. Dust from the main asteroid belt and from Jupiter-family comets (JFCs) reaches Earth's orbit with low eccentricity orbits and low inclination which results in a low geocentric velocity (12 kms^{-1} and 14.5 kms^{-1} , respectively). The eccentricity of orbits of dust from Halley-type comets (HFCs) and Oort cloud comets (OCCs) is more extreme, and these particles enter the Earth's stratosphere at higher velocities (peaks at velocities of 26 and 57 kms^{-1} , depending on particle size for HFCs and 58 kms^{-1} for OCCs) leading to higher degree of atmospheric entry heating (Carrillo-Sánchez et al., 2016; Plane et al., 2018). As models of the cosmic dust flux to Earth suggest, nearly 85–95 % of dust particles in the zodiacal dust cloud are JFC particles. Therefore, the majority of dust particles collected from Earth's stratosphere have slow entry velocities, meaning that the degree of atmospheric entry heating could also be low.

The effect of atmospheric entry heating is not strong enough to melt particles, because they are too small, but some changes in the particles due to heating can be observed. Atmospheric entry heating can evoke the formation of new, secondary mineral phases, the erasure of solar flare tracks, and the loss of volatiles. The degree of alteration or the temperatures particles experienced during atmospheric entry can be estimated by these indicators. If it is possible to determine the effects of atmospheric entry heating in the analysed particles, then primary and secondary features of IDPs can be distinguished, allowing to better constrain formation conditions of IDPs and GEMS.

Bradley et al. (2022) proposed that most IDPs are heated to temperatures above 500 °C when entering the atmosphere. The most striking textural feature is the presence of magnetite rims around GEMS which are thought to form by the oxidation of Fe-bearing phases such as Fe-metal or Fe-sulfides (Keller et al., 1996) to a different extent. They are mostly found in GEMS located at the rims of the IDPs, while those that are in the interior of particles, do not show such features. The magnetite rims in the analyzed IDPs are few nanometers thick, indicating only moderate heating during atmospheric entry (~ 600 °C). For higher temperatures (~ 850 °C), magnetite rims can have thicknesses of up to 50 nm (Keller et al., 1996). Greshake et al. (1998) analyzed effects of atmospheric entry heating experimentally by heating 50–100 μm -sized

meteorite fragments of CI chondrites Orgueil and Alais. They found that the oxidation of euhedral pyrrhotite grains to magnetite occurs in a temperature range from 500–900 °C. The sulfur loss is mostly restricted to the temperature range between 600 and 700 °C. Nevertheless, the pyrrhotite grains investigated in the CI chondrite fragments of Orgueil were euhedral grains of 15–20 μm in size. In the meteorite fragments, oxidation starts at the rims of the grains at around 600 °C, and at 700 °C there is still a core of pyrrhotite left. In the investigated IDPs, most sulfides were much smaller (up to 400 nm maximum) and rounded. Such small grains should be completely altered to magnetite if the particles experienced temperatures around 600 °C. In fact, magnetite is only found on the rims of the particles, while sulfides in the interior are still intact. This could mean that only the exterior of the particles experienced higher temperatures around 600–700 °C, while the interior remained unaltered. Some sulfides show hints of sulfur loss, most likely caused by heating during atmospheric entry. This is supported by the morphology and position of such sulfides. One sulfide in particle L2076 B5 is a small distinct crystal close to the particle rim. The part of the crystal pointing to the outside of the particle is rimmed by a Fe-rich magnetite rim, meaning that the sulfide is oxidized from the outside during atmospheric entry. The situation is similar for a sulfide in particle L2083 B1, which is a diffuse sulfide area enclosed by EA-like material to the edge of the particle. EAs are most likely formed by some process like subsolidus annealing, maybe also accompanied by sulfur loss in this case. Particles L2099 A7 and L2099 A8 have the lowest S/Si ratios of all particles (0.05 ± 0.01 , Table 1), the highest abundance of magnetite rims, and the thickest rims, demonstrating the loss of volatile S during atmospheric entry. Particle L2083 E51 shows a S/Si ratio of 0.05 ± 0.01 as A7 and A8, but this particle contains nearly no sulfides (only 1 vol%).

No hydrous mineral phases such as phyllosilicates (serpentine, saponite) were found in any of the analyzed particles. Heating might have also influenced the equilibrated aggregates. Because they show similar chemical heterogeneity as GEMS amorphous silicates, it could be assumed that there is a genetic relationship. Some process affected the GEMS grains and caused recrystallization, without strongly changing the chemical composition. In the EA areas, some minor Fe-sulfide grains are still left, while the amorphous silicates are completely recrystallized to enstatite and forsterite polycrystalline grains. Where sulfides are completely absent inside the EAs, there is a thin magnetite rim observed which suggests that Fe-metal and Fe-sulfide are completely oxidized to magnetite. Therefore, the process of transforming GEMS to EAs must have taken place in an oxidizing environment under moderate temperatures. Keller and Messenger (2009) proposed that the formation of EAs is result of thermal annealing of the amorphous GEMS precursors, maybe induced by heating events due to nebular shock waves.

Nevertheless, because the chemical composition of EAs does not change a lot, the process forming EAs must have taken place after GEMS formation, but still very early in IDP history, implying that it did not influence the particles' primitivity to a great extent. The highest abundance of EAs is found in particles L2099 A7 and L2099 A8. These are the two particles previously identified as the most altered ones based on the presence of magnetite rims and low S/Si ratios. Therefore, the abundance of EAs in IDPs can be taken as another indicator for thermal alteration.

4.1.2. Silicon oil contamination

The effect of silicon oil contamination on the element/Si ratios is another problem in the context of chemical compositions of GEMS grains. It was often argued that the silicon oil from the capturing process is not fully removed when particles are cleaned with hexane resulting in lower-than-solar element/Si ratios. If this would be the case, the measured element/Si ratios are not a primary feature of GEMS. Different methods have been used to determine the effect of silicon oil on IDPs and on their GEMS inside. Flynn et al. (2017) performed silicon XANES to examine the amount of silicon oil in GEMS. The silicon oil is dominated by Si-C bonds and therefore clearly distinguishable from the Si-O bonds of IDP silicates with a high resolution (smaller than typical GEMS diameter of 200 nm). They observed no features of silicon oil in the spectrum, inferring that the silicon oil contamination is so low that it has no influence on element/Si ratios. Another study by Messenger et al. (2012) compared IDPs collected without the use of silicon oil to those collected traditionally on silicon oil collector surfaces. The particles were captured on dry collector surfaces of polyurethane foam and were subsequently prepared the same way for TEM analysis. EDX measurements of the bulk elemental abundances and the element/Si ratios showed no systematic differences to silicon oil collected IDPs. Therefore, it can be concluded that the use of silicon oil as a collection medium has no influence on the chemical composition of particles. Moreover, Messenger et al. (2012) found GEMS to be similarly chemically heterogeneous at the nanometer-scale as previously published by other investigators (Bradley and Dai, 2009; Ishii et al., 2008; Joswiak and Brownlee, 1996; Keller and Messenger, 2011). This suggests that the chemical heterogeneity in GEMS is a pristine feature and not significantly altered using silicon oil. To exclude silicon oil contamination of GEMS grains in our samples, we performed STEM-EELS measurements on carbonaceous matter around and inside GEMS. Fig. 6c) in section 3.2.2 shows the EELS silicon areal density map of a GEMS cluster area in particle L2071 AB1 Grid3 Sec02. As it can be seen, there is a lot of silicon evident in the lower part of the map, where the carbonaceous matrix material is located that connects components. Therefore, this material might be contaminated with silicon oil. Furthermore, the silicon forms rim structures to the particle edges, especially around the GEMS cluster in the upper left of the map area but does not penetrate the GEMS cluster or the GEMS subgrains, where silicon areal density is low. This means that silicon oil contamination is present, but not inside GEMS grains. Therefore, chemical composition of GEMS amorphous silicates can be considered as unaltered by the capturing process of IDPs and the possible contamination with silicon oil.

4.2. Comparison of GEMS amorphous silicates and amorphous silicate material (ASM) in chondritic meteorites

Amorphous silicate material (ASM) is also found in the matrices of some very primitive carbonaceous chondrites such as CR, CO, and CM chondrites (Abreu, 2016; Abreu and Brearley, 2010; Dobricá and Brearley, 2020; Hopp and Vollmer, 2018; Le Guillou et al., 2015; Leroux et al., 2015; McAdam et al., 2018; Vollmer et al., 2020), that have experienced limited extent of alteration (Krot et al., 2014). It is still a matter of debate to what extent ASM in meteorites relates to GEMS amorphous silicates in terms of texture and elemental composition. Amorphous silicates in meteorites are often associated with nanosulfides (pyrrhotite, troilite,

and pentlandite), Fe-Ni-metal grains and small, crystalline grains of forsterite or enstatite in the meteorite matrix (Abreu, 2016; Abreu and Brearley, 2010; Hopp and Vollmer, 2018; Le Guillou et al., 2015). Additionally, several studies reported tiny fibers of phyllosilicates in the ASM groundmass in some matrix regions, for example in Acfer 094 or the pristine CR chondrites MET 00426 and QUE 99177, which indicate the onset of aqueous alteration reactions (Abreu and Brearley, 2010; Hopp and Vollmer, 2018; Le Guillou et al., 2015). This is a major difference to GEMS amorphous silicates, which are normally free of phyllosilicate nanofibers. We also did not observe any hints of hydration in any of our GEMS amorphous silicates such as the presence of phyllosilicate minerals.

Fig. 9 shows the chemical composition of GEMS amorphous silicates from six IDPs from this study compared to ASM compositions in various primitive meteorites from the literature. Meteoritic ASM is generally Fe-rich, while GEMS amorphous silicates are Mg-rich. Furthermore, the meteoritic ASM shows a rather wide compositional heterogeneity in Mg- and Fe-content, even among different parts of the same meteorite, e.g., GRO 95577 (Abreu, 2016; Le Guillou et al., 2015;). These differences are partly due to the diverse nature of primitive meteorites as they are often affected by brecciation, and especially the chondrite matrices are complex mixtures of fine-grained materials (Abreu and Brearley, 2010). Therefore, compositions of ASM from a specific meteorite can vary, while the overall Fe-enrichment in meteoritic ASM compared to GEMS amorphous silicates is thought to be a result of the onset of aqueous alteration of the amorphous silicates, since amorphous silicates are highly metastable (Hopp and Vollmer, 2018; Le Guillou et al., 2015). Fluids on the meteorite parent bodies might have mobilized Fe either from the ASM itself or from Fe-metal or Fe-sulfides. However, some meteorite amorphous silicates fall within the same compositional range as GEMS amorphous silicates. For example, GRO 95577 and Al Rais (Le Guillou et al., 2015) exhibit similar compositions as L2099 A7 and L2083 B1. Le Guillou et al. (2015) described these meteorites as the most altered CRs used in his study, with extended growth of crystalline phyllosilicate fibers in both samples. This can be explained by redistribution of Fe³⁺ from silicates to oxides such as magnetite with ongoing alteration. Furthermore, alteration of chondrule mesostasis might have delivered Mg and Si to the matrix, which has also changed the Fe/Mg ratio (Le Guillou et al., 2015). Therefore, the most heavily altered meteorite matrices are similar to IDP compositions due to redistribution of Fe and Mg between phases.

It is possible that GEMS amorphous silicates and meteorite ASM are genetically related because both show the same depletion in Mg compared to the solar value (grey star in Fig. 9). Hopp and Vollmer (2018) assigned this Mg-depletion to fractional condensation in the solar nebula. This is also supported by the observed matrix-chondrule complementarity in many chondrites, where the formation of chondrules depletes the solar nebula in Mg, whereas the matrix gets enriched in Si and Fe (Palme et al., 2015). This would imply that the Fe is chemically bound in the amorphous silicates itself and would not have been mobilized from the small matrix crystallites of Fe-Ni-metal or Fe-sulfide. If the Fe originates from Fe-Ni-metal and Fe-sulfide in the ASM, then a genetic relationship between GEMS amorphous silicates and ASM in meteorites is possible, because then ASM and GEMS amorphous silicates have the same (originally Mg-rich) composition. Otherwise, Fe in the meteorite ASM could be a primary feature due to condensation of more Fe-rich silicates at lower temperature as predicted by condensation theories (Grossman, 1972). The GEMS amorphous silicates then would have to condense at higher temperatures, possibly at the same time as chondrules and earlier than the meteorite ASM, depleting the gas in Mg, before it is driven to more Fe-rich compositions. Nevertheless, this would not explain why GEMS amorphous silicates are highly enriched in Si. Gas compositions should become more Si-enriched with ongoing condensation; thus, later-formed silicates should be more Si-rich as well. Taken together, based on chemical composition, it is not possible to completely reconcile whether GEMS amorphous silicates and

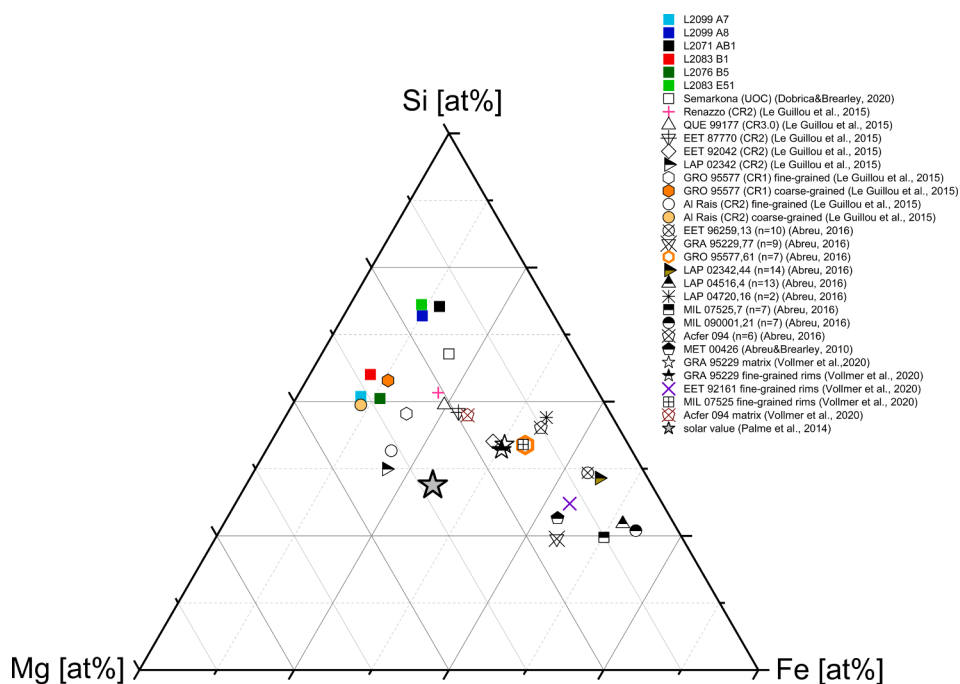


Fig. 9. Composition of GEMS amorphous silicates compared to composition of amorphous silicate material in various meteorites taken from the literature plotted in a Mg-Fe-Si ternary diagram (TEM data only).

ASM in chondrite matrices are formed by the same mechanism. The differences in composition, especially in the Mg- and Fe-content, could be a primary feature caused by fractional condensation at different times and/or temperatures or even at different locations in a nebula. Alternatively, the higher Fe-content in the meteorite ASM might be caused by more extensive aqueous alteration on the chondrite parent bodies.

4.3. Relationship of GEMS to other IDP components

In all our IDPs, GEMS are closely associated with carbonaceous material, but their relationship to other crystalline IDP components remains poorly characterized. The elongated pyroxene crystals observed in particle L2083 E51 with sizes up to 1 μm are much larger than expected for typical Mg-silicate grains from the ISM, which are 0.02 to 0.15 μm according to interstellar extinction models. Furthermore, crystalline silicates in the ISM are predicted to be rounded (Draine, 2004). In all our particles, the truly euhedral Mg-silicates, which are mostly pyroxenes, are elongated and whisker-like. Such morphologies are described as vapor phase growth forms (Bradley et al., 1983). This suggests that they have formed directly in the early solar nebula at high temperatures, because observed crystalline silicates are nearly pure enstatite composition as expected by condensation from a gas of solar composition (Grossman, 1972). Nevertheless, the dominant crystalline fraction in the investigated particles, especially in particles L2099 A7 and L2099 A8 are equilibrated aggregates. Those polycrystalline aggregate grains are mostly rounded and fit to the size predictions for ISM crystalline silicates. Chemical composition of these EA grains is very similar to GEMS amorphous silicates chemistry which could be an indication that they formed from amorphous silicate precursors by subsolidus annealing as predicted by Brownlee et al. (2005) and Keller and Messenger (2009). Formation of EAs from GEMS amorphous silicates as the dominant fraction in anhydrous IDPs also suggests that these crystalline phases form after GEMS and cannot be a chemical counterpart of the GEMS grains. Therefore, the overall chondritic composition of bulk IDPs is difficult to explain because most GEMS are subsolar for major element/Si ratios and a supersolar component is needed to counterbalance compositions. However, bulk IDP compositions tend to be subsolar in their major element/Si ratios (Sec. 3.2.1), vary by an

order of magnitude and are highly dependent on the amount and type of different mineral phases. Therefore, a supersolar component is not necessarily needed to account for bulk IDP compositions.

Furthermore, there are also compositional differences between the IDPs in this study and previous bulk IDP measurements. Schramm et al. (1989) examined the composition of 90 bulk anhydrous IDPs and calculated average element/Si ratios. Average Mg/Si, S/Si, Fe/Si, and Ni/Si ratios of our IDP samples are lower, while average Ca/Si is slightly higher. Average Al/Si ratios fit perfectly with the values of Schramm et al. (1989), but individual particles show a great range of variability in composition. The reported Mg/Si of 1.015 for bulk CP-IDPs is a magnitude higher than the average of our IDP measurements, while their Fe/Si of 0.705 for CP-IDPs is twice the average value of all our IDP analyses. These differences in bulk particle compositions might be the result of the highly diverse nature of anhydrous IDPs. Bulk chemical compositions are highly dependent on the amount and type of mineral phases within each particle and all our investigated particles differ greatly. This underlines the complex nature of these primitive components.

Sulfides are generally thought to have formed at lower temperatures than silicate minerals. The first sulfur-containing mineral to form in the early solar nebula should be stoichiometric troilite; however, pyrrhotite dominates in the investigated IDPs. Zolensky and Thomas (1995) suggested that sulfides in the solar nebula might have formed at the expense of metal during sulfidation, with an initial sulfide rim exfoliating from the metal core. As soon as the metal is no longer in equilibrium with the troilite rim, the sulfide might have been further sulfurized by interaction with surrounding H_2S gas, and pyrrhotite is formed. Pyrrhotite is also the dominant sulfide found as nanoinclusions in GEMS (Dai and Bradley, 2001). Both GEMS amorphous silicate and GEMS inclusions could form from a gas of solar composition by fractional crystallization. Otherwise, it is possible that nanosulfides formed by UV irradiation of H_2S ice mantles accreted by dust grains in dense molecular cloud cores as shown by Cazaux et al. (2022), which could produce a variety of sulfur-bearing species found in comets such as 67P/Churyumov-Gerasimenko (Calmonte et al., 2016). It is therefore likely that anhydrous IDPs thought to originate from comets have obtained their sulfur in a similar way by irradiation of such precursor ices.

To conclude, a genetic relationship of GEMS to euhedral pyroxene crystals in IDPs is not verified, because pyroxene compositions and textures point to a high temperature formation, which is too hot for GEMS amorphous silicates. The compositional relationship of GEMS and equilibrated aggregates (EAs) is striking, because it supports EA formation by recrystallization of GEMS material. A chemical complementarity of GEMS amorphous silicates and crystalline components in IDPs as observed in carbonaceous chondrites cannot be proven. GEMS studied here are subsolar for most major element/Si ratios, as well as their host IDPs, although there is great variability in composition depending on the type and amount of different mineral phases. The picture is not that clear for sulfides in IDPs and sulfide nanoinclusions in GEMS. They most likely formed by sulfidation of preexisting metal grains, but whether this sulfidation occurred in a nebular environment or by irradiation of sulfur-bearing ice mantles, remains ambiguous.

4.4. Formation theories of GEMS

GEMS are a fundamental component of interplanetary dust particles, but it is still unclear, how and where GEMS have formed. Because cometary dust is mostly unaffected by any secondary alteration processes on the parent body, it is assumed that components of cometary IDPs can give insights into the early history of the solar system and its building blocks. GEMS are therefore a promising candidate, because they contain amorphous silicates, an important component of many astrophysical environments such as the interstellar medium (ISM) and are also found in the matrices of some very primitive meteorites.

Compositional analyses of the truly amorphous silicate inside GEMS make it possible to compare this material to the amorphous silicate material within meteorite matrices and the ISM and might reveal a possible genetic relationship. Furthermore, compositions of GEMS amorphous silicates reflect formation processes, either in the early solar nebula or as a fundamental component of previous star generations.

Up to now, different formation theories are proposed. GEMS are either considered to be solar system material that condensed from the solar nebula by non-equilibrium condensation processes (Keller and Messenger, 2011) or are formed via irradiation of crystalline precursor grains in the interstellar medium (Bradley and Dai, 2004). Here we present a formation scenario of GEMS based on our new results and seen in the context of other IDP components.

Most GEMS in our study are rounded or at least oval objects of around 100–500 nm in size. The size distribution for silicate grains in the ISM peaks at 300 nm (Draine, 2004), which fits with GEMS size. Furthermore, most models of ISM dust composition predict a mixture of graphite, silicates, Polycyclic Aromatic Hydrocarbons (PAHs), and amorphous silicates and carbon (Desert et al., 1990; Li and Greenberg, 1997; Mathis et al., 1977; Siebenmorgen et al., 2014; Weingartner and Draine, 2001; Zubko et al., 1999). But in a formation scenario as proposed by Bradley and Dai (2004), a high abundance of crystalline precursor grains is needed to be irradiated. Crystalline grains make up only 1.1 to 2.2 % of the silicates in the ISM as inferred from spectral observations (Kemper et al., 2005). This fraction is far too small to act as precursors of GEMS grains and cannot explain the high abundance of GEMS (up to 40 vol% in the particles analyzed here) in most CP-IDPs. Ishii et al. (2018) proposed a multi-stage formation based on the distinction of two generations of carbon in EDX and EELS measurements. In this scenario, GEMS formation takes place in dense molecular cloud environments partly shielded from radiation. On silicate precursor grains, organic-rich icy mantles were adsorbed and formed the proto-GEMS. During cycling in and out of the molecular cloud, more than one layer of carbon would form around the early GEMS grains (Ishii et al., 2018). The first carbon species found is a higher-density carbon surrounding GEMS and GEMS subgrains and the second forms the semicontinuous matrix with lower density that connects GEMS and all other IDP components. As shown by our EDX and EELS measurements, we found higher signal intensities for carbon around GEMS in the EDX

maps (Fig. 5). This might correspond to a higher-density carbon species, but this cannot be completely deduced from the elemental maps alone. The EELS carbon areal density map of a cluster GEMS (Fig. 6) confirms higher number of carbon atoms around GEMS subgrains than in the diffuse carbonaceous matrix material. The higher carbon areal density is also found in a carbon nanoglobule (lower edge of GEMS cluster in Fig. 6), which suggest a possible genetic relationship between the GEMS carbon and carbon nanoglobules in IDPs.

The irradiation of organic mantles also causes chemical fractionation at temperatures as low as ~ 20 K and subsequent isotopic enrichment in ^{15}N . This process might result in enrichments of ^{15}N by about a few hundred or even ≥ 1000 ‰ (Chan et al., 2020; Floss et al., 2004; Floss et al., 2006). In our analyses, all IDPs show $\delta^{15}\text{N}$ values of around +100 ‰, with the most prominent hotspot in L2071 AB1 Grid2 Sec07 with $\delta^{15}\text{N} = 1177 \pm 86$ ‰. Nevertheless, measurements of other N-bearing subregions in the same particle show $\delta^{15}\text{N}$ values of -10 and $+120$ ‰, respectively. This supports the assumption, that bulk IDPs are complex mixtures of material originating from different locations or times in the solar nebula or even before in the protosolar molecular cloud. The only particle section showing terrestrial $\delta^{15}\text{N}$ values close to 0 ‰ is L2083 B1 Grid3 Sec07 ($\delta^{15}\text{N} = 2 \pm 8$ ‰). This section contains less pore space than other sections of the same particle and has a higher fraction of crystalline components. The crystalline components are mostly EAs with some GEMS-like areas in between. These GEMS grains also show hints of recrystallization and exhibit magnetite rims of 10 to 20 nm thickness, but still retained their GEMS-like appearance. This indicates that the section experienced some degree of atmospheric entry heating, although not to a great extent. The thermal alteration might have also erased the organic matter's anomalous nitrogen isotopic signature. Riebe et al. (2020) found in heating experiments that $\delta^{15}\text{N}$ is decreasing with increased heating, but the effect is small at temperatures below 800 °C. Therefore, the effect on the $\delta^{15}\text{N}$ composition is not the main reason for the terrestrial values of this particle section. The section might contain material with lower $\delta^{15}\text{N}$ intermixed with those with higher $\delta^{15}\text{N}$ at the nanoscale. We conclude that this section might have experienced some alteration that lowered $\delta^{15}\text{N}$ but also contains material with a different nitrogen isotopic signature. The adjacent section L2083 B1 Grid3 Sec08 has a $\delta^{15}\text{N}$ of 110 ± 13 ‰. Therefore, differences in nitrogen isotopic compositions of the carbonaceous material vary at the nanometer scale, because sections are only 70 nm thick.

Organic mantles are not only described around GEMS grains, but also on a presolar forsterite grain from a supernova in an anhydrous cluster IDP (Messenger et al., 2005). In none of the IDPs analyzed in this study, carbonaceous rims were observed around isolated crystals such as Mg-silicates. They either could have never been present or could have been destroyed before accretion into final IDP parent bodies. The grain found by Messenger et al. (2005) was identified to be presolar, therefore, it likely acquired the organic mantle during passage from a circumstellar environment into the solar system. This shows that high-temperature components, such as this forsterite grain, can be overprinted or encapsulated in ^{15}N -rich organic material. The presence of organic mantles is therefore not a clear indicator of a specific formation environment of grains, because the mantles can also be acquired long after grain formation. Therefore, GEMS can also form in higher-T environment, before final aggregation of subgrains.

Proto-GEMS do not necessarily have to form in a cold environment by irradiation processing (Bradley and Dai, 2004) but can also condense from a gas of solar composition via non-equilibrium fractional crystallization in a circumstellar environment and were subsequently transported into the solar system. The fractional condensation scenario would best explain the observed chemical trends in the GEMS amorphous silicate with element/Si ratios depleted compared to the solar value. Furthermore, the overall chemical heterogeneity cannot be explained by intensive irradiation, because this would result in homogenization of grains in the ISM. If those grains formed by condensation, this would start with Fe-metal nanoparticles acting as nuclei for the silicate

material to condense (Grossman, 1972; Keller and Messenger, 2011). The silicates would then start to condense at temperatures just below the glass transition temperature of around 1000 K to explain the amorphous nature of the silicate material. The extension to more Si-enriched compositions in the GEMS amorphous silicates can be explained by ongoing condensation over a broad temperature interval (Grossman, 1972; Keller and Messenger, 2011). Laboratory experiments with mixtures of Mg and SiO performed in hydrogen atmosphere, at a pressure of 10^{-3} bar, and temperatures around 800 K have proven that it is possible to produce amorphous silicates (Day and Donn, 1978). A recent study by Matsuno et al. (2021) has shown that it is possible to condense amorphous silicate particles with multiple Fe inclusions similar to GEMS textures from condensation of high-temperature gases under intermediate redox conditions. However, sulfur was not included in these experiments. Enju et al. (2022) used an induction thermal plasma system and the elements Mg, Fe, Si, O, and S to recreate GEMS in the laboratory under different redox conditions. They found that under intermediate redox conditions, an amorphous Fe-poor silicate material with Fe-metal nanoinclusions formed. These experiments demonstrate that GEMS can condense from high-temperature gases under intermediate redox conditions. We conclude that this does not necessarily have to be the solar nebula, but could also be a circumstellar environment, because the acquisition of carbon rims most likely happened in a multi-stage process during cycling in and out of the protosolar molecular cloud or the solar nebula.

5. Conclusions

A detailed investigation of texture and composition of eight different anhydrous CP-IDPs and their silicate and organic components was performed (L2099 A1a, L2099 A7, L2099 A8, L2071 AB1, U2153 B4, L2083 B1, L2076 B5, and L2083 E51). The combined petrographical and chemical investigation of IDPs and especially their GEMS component led us to conclude the following results:

- The presence of magnetite rims of a few nanometers on particle edges in L2099 A7 and L2099 A8 and the preservation of small sulfide grains (up to 400 nm) inside these IDPs indicates only moderate heating (~ 600 °C) during atmospheric entry. These two IDPs also have the lowest S/Si ratio of all investigated particles due to loss of volatile sulfur and are dominated by EAs, which are also thought to form via a secondary subsolidus annealing process. The absence of such features in the other six studied IDPs can be used as an indicator for primitiveness of particles.
- 105 ROIs of GEMS amorphous silicates have been analyzed regarding their chemical composition. They are all subsolar for major elements and show a wide chemical heterogeneity from enstatite-normative composition up to Si-enriched. This chemical trend supports a fractional condensation origin for GEMS and does not match with intensive homogenization via sputtering in the ISM.
- The contamination of GEMS with silicon oil can be excluded. The silicon EELS areal density map shows that silicon oil is present in the carbonaceous matrix material and around GEMS rims, but did not penetrate the interior of GEMS grains. Therefore, element/Si ratios are not polluted by silicon oil and are a primary feature of GEMS grains.
- GEMS show the same compositional heterogeneity as EAs with subsolar major element/Si ratios, suggesting that EAs formed from GEMS during alteration. Therefore, EAs form after GEMS and cannot be a counterpart of GEMS to account for overall chondritic composition of bulk IDPs. However, our analyses showed that bulk IDPs are also subsolar for major element/Si ratios, so a supersolar component is not necessarily needed.
- Nearly all GEMS are aggregates of smaller subgrains as seen from Mg and Si elemental maps. The subgrains are as small as 20 nm in diameter and the size and abundance of nanoinclusions of Fe-Ni-metal and sulfides varies between individual subgrains. These

textures point to agglomeration after formation of the smallest GEMS subgrains.

- Between GEMS subgrains, high-density carbon is found. This carbon has a higher density than the carbonaceous matrix material in IDPs as seen in carbon EELS areal density maps. It is also located around GEMS clusters, sometimes even as double-rim structures. The occurrence of such features further supports agglomeration in the ISM or the early solar nebula.

CRediT authorship contribution statement

Birgit Schulz: Conceptualization, Data curation, Formal analysis, Investigation, Methodology, Project administration, Validation, Visualization, Writing – original draft, Writing – review & editing. **Christian Vollmer:** Conceptualization, Funding acquisition, Project administration, Resources, Supervision. **Jan Leitner:** Data curation, Investigation, Resources, Software, Visualization, Writing – review & editing. **Lindsay P. Keller:** Investigation, Methodology, Resources, Validation, Writing – review & editing. **Quentin M. Ramasse:** Data curation, Investigation, Resources, Software, Writing – review & editing.

Declaration of competing interest

The authors declare that they have no known competing financial interests or personal relationships that could have appeared to influence the work reported in this paper.

Acknowledgments

We thank NASA Astromaterials Acquisition & Curation Office for providing IDP samples, Ursula Heitmann for additional ultramicrotome preparation of samples for further analysis, as well as Elmar Gröner and Philipp Schuhmann for technical support on the NanoSIMS. We also acknowledge funding of the Thermo Fisher TEM “Themis” by the DFG via the Major Research Instrumentation Program under INST 211/719-1. This project is funded by the DFG (VO1816/5-1).

Appendix A. Supplementary material

The supplementary material contains all underlying research data. Furthermore, there are additional figures provided showing an example for choosing ROIs in a single aggregate GEMS grain and overview of a particle with different carbon generations (carbonaceous matrix material and higher-density carbon around GEMS subgrains) in IDPs.

Supplementary material to this article can be found online at <https://doi.org/10.1016/j.gca.2024.06.013>.

References

- Abreu, N.M., 2016. Why is it so difficult to classify Renazzo-type (CR) carbonaceous chondrites? – Implications from TEM observations of matrices for the sequences of aqueous alteration. *Geochim. Cosmochim. Acta* 194, 91–122.
- Abreu, N.M., Brearley, A.J., 2010. Early solar system processes recorded in the matrices of two highly pristine CR3 carbonaceous chondrites, MET 00426 and QUE 99177. *Geochim. Cosmochim. Acta* 74, 1146–1171.
- Asplund, M., Amarsi, A.M., Grevesse, N., 2021. The chemical make-up of the Sun: A 2020 vision. *A&A* 653, A141.
- Berger, E.L., Zega, T.J., Keller, L.P., Lauretta, D.S., 2011. Evidence for aqueous activity on comet 81P/Wild2 from sulfide mineral assemblages in Stardust samples and CI chondrites. *Geochim. Cosmochim. Acta* 75, 3501–3513.
- Bradley, J.P., 1988. Analysis of chondritic interplanetary dust in thin-sections. *Geochim. Cosmochim. Acta* 52, 889–900.
- Bradley, J.P., 1994. Chemically anomalous, preaccretionally irradiated grains in interplanetary dust from comets. *Science* 265, 925–929.
- Bradley J.P., Dai Z.R., 2004. Mechanism of formation of glass with embedded metal and sulfides. *ApJ* 617, 650–655.
- Bradley, J.P., Brownlee, D.E., Veblen, D.R., 1983. Pyroxene whiskers and platelets in interplanetary dust: Evidence of vapour phase growth. *Nature* 301, 473–477.
- Bradley, J.P., Dai, Z.R., 2009. Analytical SuperSTEM for extraterrestrial materials research. *Meteorit. Planet. Sci.* 44, 1627–1642.

- Bradley, J.P., Brownlee, D.E., Fraundorf, P., 1984. Discovery of nuclear tracks in interplanetary dust. *Science* 226, 1432–1434.
- Bradley, J.P., Ishii, H.A., Bustillo, K., Ciston, J., Oglione, R., Stephan, T., Brownlee, D.E., Joswiak, D.J., 2022. On the provenance of GEMS, a quarter century post discovery. *Geochim. Cosmochim. Acta* 335, 323–338.
- Bradley, J.P., 2014. Early Solar Nebula Grains - Interplanetary dust particles. In: Holland, H.D., Turekian, K.K. (Eds.), *Treatise on Geochem.*, pp. 287–308.
- Brownlee, D.E., 1985. Cosmic dust: collection and research. *Annu. Rev. Earth Planet. Sci.* 13, 147–173.
- Brownlee, D.E., Joswiak, D.J., Bradley, J.P., Matrajt, G., Wooden, D.H., 2005. Cooked GEMS - Insights into the hot origins of crystalline silicates in circumstellar disks and cold origins of GEMS. *Lunar Planet. Sci. 36*, #2391.
- Brownlee D.E., 2014 Comets. In *Treatise on Geochemistry* (eds. Holland H.D. and Turekian K. K.), 335–363.
- Calmonte, U., Altwegg, K., Balsiger, H., Berthelier, J.J., Bieler, A., Cessateur, G., Dhooche, F., van Dishoeck, E.F., Fiethe, B., Fuselier, S.A., Gasc, S., Gombosi, T.I., Hässig, M., Le Roy, L., Rubin, M., Sémon, T., Tzou, C.-Y., Wampfler, S.F., 2016. Sulphur-bearing species in the coma of comet 67P/Churyumov-Gerasimenko. *MNRAS* 462, S253–S273.
- Carrillo-Sánchez, J.D., Nesvorný, D., Pokorný, P., Janches, D., Plane, J.M.C., 2016. Sources of cosmic dust in the Earth's atmosphere. *Geophys. Res. Lett.* 43, 11979–11986.
- Cazaux S., Carrascosa H., Muñoz Caro G. M. Caselli P., Fuente A., Navarro-Almida D., Riviére-Marichalar P., 2022. Photoprocessing of H2S on dust grains. *A&A* 657, A100.
- Chan, Q.H.S., Franchi, I.A., Zhao, X., Stepant, A., Wright, I.P., Alexander, C.M.O., 2020. Organics preserved in anhydrous interplanetary dust particles: pristine or not? *Meteorit. Planet. Sci.* 55, 1320–1348.
- Dai, Z.R., Bradley, J.P., 2001. Iron-nickel sulfides in anhydrous interplanetary dust particles. *Geochim. Cosmochim. Acta* 65, 3601–3612.
- Day, K.L., Donn, B., 1978. An experimental investigation of the condensation of silicate grains. *ApJ Lett.* 222, L45–L48.
- Desert, F.-X., Boulanger, F., Puget, J.L., 1990. Interstellar dust models for extinction and emission. *A&A* 237, 215–236.
- Dobricá, E., Brearley, A.J., 2020. Amorphous silicates in the matrix of Semarkona: The first evidence for the localized preservation of pristine matrix materials in the most unequilibrated ordinary chondrites. *Meteorit. Planet. Sci.* 55, 649–668.
- Draine, B.T., 2004. *Interstellar Dust Models*. ASP Conf. Series 309, 691–708.
- Enju, S., Kawano, H., Tsuchiyama, A., Kim, T.H., Takigawa, A., Matsuno, J., Komaki, H., 2022. Condensation of cometary silicate dust using an induction thermal plasma system. *A&A* 661, A121.
- Floss, C., Stadermann, F.J., Bradley, J.P., Dai, Z.R., Bait, S., Graham, G., 2004. Carbon and nitrogen isotopic anomalies in an anhydrous interplanetary dust particle. *Science* 303, 1355–1358.
- Floss, C., Stadermann, F.J., Bradley, J.P., Dai, Z.R., Bait, S., Graham, G., Lea, A.S., 2006. Identification of isotopically primitive interplanetary dust particles: A NanoSIMS isotopic imaging study. *Geochim. Cosmochim. Acta* 70, 2371–2399.
- Flynn, G.J., 1990. The near-earth enhancement of asteroidal over cometary dust. *Proceed. Lunar Planet. Sci.* 20, 363–371.
- Flynn, G.J., 1996. Sources of 10 micron interplanetary dust: the contribution from the Kuiper Belt. *ASP Conference Series* 104, 171–175.
- Flynn, G.J., Wirick, S., Butterworth, A.L., Gainsforth, Z., Westphal, A.J., Kaulich, B., Araki, T., Abyaneh, M., Tylliszczak, T., 2017. Silicon Xanes Assessment of the Silicone Oil Content of GEMS in IDPs. *Lunar Planet. Sci.* 48, #1059.
- Greshake, A., 1997. The primitive matrix components of the unique carbonaceous chondrite Acfer 094: a TEM study. *Geochim. Cosmochim. Acta* 61, 437–452.
- Greshake, A., Klöck, W., Arndt, P., Maetz, M., Flynn, G.J., Bait, S., Bischoff, A., 1998. Heating experiments simulating atmospheric entry heating of micrometeorites: Clues to their parent body sources. *Meteorit. Planet. Sci.* 33, 267–290.
- Grossman, L., 1972. Condensation in the primitive solar nebula. *Geochim. Cosmochim. Acta* 36, 597–619.
- Hillion, F., Kilburn, M.R., Hoppe, P., Messenger, S., Weber, P.K., 2008. The effect of QSA on S, C, O and Si isotopic ratio measurements. *Geochim. Cosmochim. Acta* 72, A377.
- Hopp, T., Vollmer, C., 2018. Chemical composition and iron oxidation state of amorphous matrix silicates in the carbonaceous chondrite Acfer 094. *Meteorit. Planet. Sci.* 53, 153–166.
- Ishii, H.A., 2019. Comparison of GEMS in interplanetary dust particles and GEMS-like objects in a Stardust impact track in aerogel. *Meteorit. Planet. Sci.* 54, 202–219.
- Ishii, H.A., Bradley, J.P., Dai, Z.R., Chi, M., Kearsley, A.T., Burchell, M.J., Browning, N. D., Molster, F., 2008. Comparison of comet 81P/Wild2 dust with interplanetary dust from comets. *Science* 319, 447–450.
- Ishii, H.A., Bradley, J.P., Bechtel, H.A., Brownlee, D.E., Bustillo, K.C., Ciston, J., Cuzzi, J. N., Floss, C., Joswiak, D.J., 2018. Multiple generations of grain aggregation in different environments preceded solar system body formation. *PNAS* 115, 6608–6613.
- Joswiak D.J., Brownlee, D.E., 1996. Systematic analyses of major element distributions in GEMS from high speed IDPs. *Lunar Planet. Sci.* 27, #1313.
- Keller, L.P., Flynn, G.J., 2022. Evidence for a significant Kuiper belt dust contribution to the zodiacal cloud. *Nat. Astron.* 6, 731–735.
- Keller, L.P., Messenger, S., 2009. Equilibrated aggregates in cometary IDPs: Insights into the crystallization process in protoplanetary disks. *Lunar Planet. Sci.* 40, #2121.
- Keller, L.P., Messenger, S., 2011. On the origin of GEMS grains. *Geochim. Cosmochim. Acta* 75, 5336–5365.
- Keller, L.P., Thomas, K.L., McKay, D.S., 1996. Mineralogical changes in IDPs resulting from atmospheric entry heating. *Int. Astronom. Union Colloquium* 150, 295–298.
- Keller, L.P., 2020. Chemical complementarity in cometary dust particles. *Goldschmidt*, #1270.
- Kemper, F., Vriend, W.J., Tielens, A., 2005. Erratum: “The Absence of Crystalline Silicates in the Diffuse Interstellar Medium” (*ApJ*, 609, 826 [2004]). *ApJ* 633, 534.
- Krot A. N., Keil K., Scott E. R. D., Goodrich C.A., Weisberg M.K., 2014 Classification of meteorites and their genetic relationships. In: *Treatise on Geochemistry* (eds: Holland H. D. and Turekian K. K.), 1–63.
- Le Guillou, C., Changela, H.G., Brearley, A.J., 2015. Widespread oxidized and hydrated amorphous silicates in CR chondrites matrices: Implications for alteration conditions and H2 degassing of asteroids. *Earth Planet. Sci. Lett.* 420, 162–173.
- Leroux, H., Cuvillier, P., Zanda, B., Hewins, R.H., 2015. GEMS-like material in the matrix of the Paris meteorite and the early stages of alteration of CM chondrites. *Geochim. Cosmochim. Acta* 170, 247–265.
- Li, A., Greenberg, J.M., 1997. A unified model of interstellar dust. *A&A* 323, 566–584.
- Mathis, J.S., Rumpl, W., Nordsieck, K.H., 1977. The size distribution of interstellar grains. *ApJ* 217, 425–433.
- Matsuno, J., Tsuchiyama, A., Watanabe, T., Tanaka, M., Takigawa, A., Enju, S., Koike, C., Chihara, H., Miyake, A., 2021. Condensation of glass with multimetal nanoparticles: implications for the formation process of GEMS grains. *ApJ* 911, 47.
- McAdam, M.M., Sunshine, J.M., Howard, K.T., Alexander, C.M., Timothy, J., Schelte, J., 2018. Spectral evidence for amorphous silicates in least-processed CO meteorites and their parent bodies. *Icarus* 306, 32–49.
- Messenger, S., Keller, L.P., Lauretta, D.S., 2005. Supernova olivine from cometary dust. *Science* 309, 737–741.
- Messenger, S., Keller, L.P., Nakamura-Messenger, K., Clemett, S.J., 2012. Pristine stratospheric collections of cosmic dust. *Lunar Planet. Sci.* 43, #2696.
- Nakamura-Messenger, K., Clemett, S.J., Messenger, S., Keller, L.P., 2011. Experimental aqueous alteration of cometary dust. *Meteorit. Planet. Sci.* 46, 843–856.
- Ohtaki, K.K., Ishii, H.A., Bradley, J.P., Villalon, K.L., Davis, A.M., Stephan, T., Bustillo, K. C., Ciston, J., 2021. Search for meteoritic GEMS I: Comparison of amorphous silicates in Paris and Acfer 094 chondrite matrices and in anhydrous chondritic interplanetary dust particles. *Geochim. Cosmochim. Acta* 310, 320–345.
- Palme, H., Lodders, K., Jones A.P., 2014. Solar system abundances of the elements. In: *Treatise on Geochemistry* (eds: Holland H. D. and Turekian K. K.), 15–36.
- Palme, H., Hezel, D.C., Ebel, D.S., 2015. The origin of chondrules: Constraints from matrix composition and matrix-chondrule complementarity. *Earth Planet. Sci. Lett.* 411, 11–19.
- Pearson, V.K., Sephton, M.A., Franchi, I.A., Gibson, J.M., Gilmour, I., 2006. Carbon and nitrogen in carbonaceous chondrites: elemental abundances and stable isotopic compositions. *Meteorit. Planet. Sci.* 41, 1899–1918.
- Plane, J.M.C., Flynn, G.J., Määttä, A., Moores, J.E., Poppe, A.R., Carrillo-Sanchez, J. D., Listowski, C., 2018. Impacts of cosmic dust on planetary atmospheres and surfaces. *Space Sci. Rev.* 214, 1–42.
- Riebe, M., Foustoukos, D.I., Alexander, C., Steele, A., Cody, G.D., Mysen, B.O., Nittler, L. R., 2020. The effects of atmospheric entry heating on organic matter in interplanetary dust particles and micrometeorites. *Earth Planet. Sci. Lett.* 540, 116226.
- Schramm, L.S., Brownlee, D.E., Wheelock, M.M., 1989. Major element composition of stratospheric micrometeorites. *Meteorit. Planet. Sci.* 24, 99–112.
- Siebenmorgen, R., Voshchinnikov, N.V., Bagnulo, S., 2014. Dust in the diffuse interstellar medium - extinction, emission, linear and circular polarisation. *A&A* 561, A82.
- Slodzian, G., Hillion, F., Stadermann, F.J., Zinner, E., 2004. QSA influences on isotopic ratio measurements. *App. Surf. Sci.* 231–232, 847–877.
- Verbeeck, J., Van Aert, S., Bertoni, G., 2006. Model-based quantification of EELS spectra: Including the fine structure. *Ultramicroscopy* 106, 976–980.
- Villalon, K.L., Ohtaki, K.K., Bradley, J.P., Ishii, H.A., Davis, A.M., Stephan, T., 2021. Search for meteoritic GEMS II: Comparison of inclusions in amorphous silicates from the Paris chondrite and from anhydrous chondritic interplanetary dust particles. *Geochim. Cosmochim. Acta* 310, 346–362.
- Vollmer, C., Pelka, M., Leitner, J., Janssen, A., 2020. Amorphous silicates as a record of solar nebula and parent body processes – A transmission electron study of fine-grained rims and matrix in three Antarctic CR chondrites. *Meteorit. Planet. Sci.* 55, 1491–1508.
- Weingartner, J.C., Draine, B.T., 2001. Dust grain-size distributions and extinction in the Milky Way, Large Magellanic Cloud, and Small Magellanic Cloud. *ApJ* 548, 296–309.
- Zolensky, M.E., Thomas, K.L., 1995. Iron and iron-nickel sulfides in chondritic interplanetary dust particles. *Geochim. Cosmochim. Acta* 59, 4707–4712.
- Zubko, V.G., Smith, T.L., Witt, A.N., 1999. Silicon nanoparticles and interstellar extinction. *ApJ Lett.* 511, L57–L60.